DESIGN OF METAMATERIAL-BASED NANOSTRUCTURES FOR 5G APPLICATIONS & THERMAL RADIATION MANAGEMENT

A THESIS SUBMITTED TO

THE GRADUATE SCHOOL OF ENGINEERING AND SCIENCE

OF BILKENT UNIVERSITY

IN PARTIAL FULFILLMENT OF THE REQUIREMENTS FOR

THE DEGREE OF

MASTER OF SCIENCE

IN

ELECTRICAL AND ELECTRONICS ENGINEERING

By

Ekin Bircan Boşdurmaz

June 2023

DESIGN OF METAMATERIAL-BASED NANOSTRUCTURES FOR 5G APPLICATIONS & THERMAL RADIATION MANAGEMENT
By Ekin Bircan Boşdurmaz
June 2023

We certify that we have read this thesis and that in our opinion it is fully adequate, in scope and in quality, as a thesis for the degree of Master of Science.

Ekmel Özbay(Advisor)

Orhan Aytür

İbrahim Tuna Özdür

Approved for the Graduate School of Engineering and Science:

Orhan Arıkan
Director of the Graduate School

ABSTRACT

DESIGN OF METAMATERIAL-BASED NANOSTRUCTURES FOR 5G APPLICATIONS & THERMAL RADIATION MANAGEMENT

Ekin Bircan Boşdurmaz
M.S. in Electrical and Electronics Engineering
Advisor: Ekmel Özbay
June 2023

The properties of natural materials can be the only limiting factor in today's technologies. For this, researchers in the last decades found that engineering the features of naturally occurring materials in the subwavelength scales can drastically change their properties. These materials beyond the natural ones are called "metamaterials", where "meta" means "beyond" in Greek. Although the fabrication of these materials can be quite challenging, clever designs and exploitation of physical phenomena can lead to tunable responses, eliminating the need for multiple structures. Here, different strategies for designing tunable meta-surfaces for a wide range of applications will be presented by giving two examples. These applications are namely: 1. Graphene-based Metasurface Absorber for the Active and Broadband Manipulation of Terahertz Radiation, 2. Adaptive Thermally Tunable Radiative Cooling with Angle Insensitivity Using Phase-Change Material-Based Metasurface.

Keywords: Terahertz Radiation, Radiative Cooling, Metasurface, Metamaterial, Visible, Infrared, Graphene, Phase-Change Material..

ÖZET

5G UYGULAMALARI VE TERMAL RADYASYON YONETIMI ICIN METAMALZEME TABANLI NANOYAPI TASARIMI

Ekin Bircan Boşdurmaz
Elektrik ve Elektronik Mühendisliği, Yüksek Lisans
Tez Danışmanı: Ekmel Özbay
Haziran 2023

Doğal malzemelerin karakteristik özellikleri, günümüz teknolojilerinin gelişmesinin önündeki tek kısıtlayıcı faktör olabilmektedir. Bu darboğazın önüne geçebilmek için günümüz araştırmacıları, doğal malzemelerin dalgaboyundan daha kısa ölçeklerde şekillendirilmesi ve tasarlanması ile bu doğal malzemelerin özelliklerini büyük ölçüde değiştirilebileceğini göstermiştir. Bu malzemeler, literatürde "metamalzeme" olarak bilinmektedir ve "meta" Yunanca'da "ötesi" anlamına gelmektedir. Bu malzemelerin üretimlerinin çok karışık ve zorluca süreçler olabilmesine karşılık, akıllıca tasarımlar ve fiziksel süreçlerin istenilen sonuç lehine kullanılması ayarlanabilir optik yapıların, birden fazla nanoyapıya ihtiyaç duymadan gerçekleştirilebilmesini sağlamıştır. Bu tezde, çeşitli uygulamalar için tasarlanmış ayarlanabilir metayüzeyler, iki örnek ile sunulmuştur. Bu örnekler: 1. Terahertz Radyasyonun Aktif ve Genişbant Manipülasyonu için Grafen tabanlı Metayüzey Soğurucu, 2. Faz Değişimli Malzeme Tabanlı Metayüzey Kullanarak Açı Duyarsızlığı ile Adaptif Termal Olarak Ayarlanabilen Işınımlı Soğutma.

Anahtar sözcükler: Terahertz Işınımı, Işınımlı Soğutma, Metayüzey, Metamalzeme, Görünür, Kızılötesi, Grafen, Faz Değişimli Malzeme..

Acknowledgement

First of all, I would like to thank to my academic advisor Prof. Ekmel Ozbay for his support from my undergraduate research times until the completion of my graduate studies at NANOTAM. Also, I would like Prof. Orhan Aytür and Prof. İbrahim Tuna Özdür for being in my thesis committee and providing feedbacks to improve my thesis.

I would like to thank BTK, 5G and Beyond Scholarship Program, and Vodafone for supporting my studies.

For their support and guidance during my research I would like to thank Dr. Hodjat Hajian and Dr. Amir Ghobadi. I have learned lots of things from you.

I owe my deepest gratitude to whole NANOTAM family. From my officemate Türkan Gamze Ulusoy Ghobadi to Oğuz Odabaşı, Tayfur Kaya, Volkan Ertürk, Veysel Erçağlar, Ebru Buhara, Zahra Rahimian Omam, Ataollah Kalantari Osgouei, Mahmut Can Soydan and Salahuddin Zafar. I would like to thank Tuğçe Kafdağlı, Gamze Seğmenoğlu, Mehmet Özgür, and Enis Galip Erdöl always helping with any problems.

I also would like to thank the UNAM family, where my scientific journey began as a little sophomore student. Especially the cleanroom and characterization team: Taha Ilıkkan, Abdullah Kafadenk, Esra Arman Karaaslan, and Semih Bozkurt.

As a candidate scientist, I try to learn from everyone that I met and talked. I would like to thank all the people that I have even a little chat during my Bilkent adventure. If I forgot to include your name here, please forgive me. Let's start with my great instructors: Ahmet Züfer Eriş, Ali Ulvi Yılmazer, Cemal Yalabık, Ceyhun Bulutay, Mehmet Özgür Oktel, Seymur Jahangirov, Zafer Gedik, Oğuz Gülseren, Ceren Sibel Sayın, Abdullah Atalar. From those great people, I would like to thank, -here we go, a long list-, Elif Sıla Akbulut, Anıl Taylan Öner, Enise Kartal, Asiye İrem Deşdemir, Elif Mercan, Bilge Banu Yağcı, Murat A. Güngen,

Beliz Doğukaya, Mehmet Bütan, Melike Tombaz, Yusuf Aslan, Aslı Bozkurt, Mahmud Sami Aydın, Şeyma Kılıç, Alkım Şentürk, Melisa Tanrıkulu, Deniz İlke Silistre, Ece Kılıç, AstroBilkent, Neriman'ın Schrödingeri, 123 and list goes on ... I would like to thank to Ekin Taşkın, Kübra Fansa, Sezan Mert, Meyra Can, Selinay Temiz for not leaving me after high school :).

Finally, I would like to thank my family, starting from my grandmother, to my mother Neslihan, my father Yetkin, and my brother-in-arms Burak for being with me and their support all the time.

Now, "allow me to write my final words..." for this "hunt for tricks of light...". I believe no thesis can be written without good music. So let me share some quotes from my favorite songs.

"Man, he took his time in the sun
Had a dream to understand
A single grain of sand
He gave birth to poetry
But one day'll cease to be
Greet the last light of the library"

The Greatest Show on Earth
Nightwish

"Can we find the lightning
that shines inside our mind?
Can we fight the dark side,
we've all been trying to hide?"

The Skeleton Key
Epica

Contents

List of Figures

Chapter 1

Introduction

This chapter is on part reprinted with permission from: **Ekin Bircan Boşdurmaz**, Hodjat Hajian, Veysel Erçağlar, and Ekmel Özbay, Journal of the Optical Society of America B, vol. 38, no. 9. The Optical Society, p. C160, Aug. 10, 2021. doi: 10.1364/josab.427975.

1.1 Background

In recent years, metamaterials have emerged as a promising type of engineered materials that exhibit unique and exotic properties not found in natural materials [1–3]. Metamaterials consist of artificially designed structures with subwavelength features, allowing for the manipulation of electromagnetic waves and thermal radiation [4, 5]. Controlling the behavior of light and heat at the nanoscale has opened up new possibilities for a wide range of applications, including communication [6, 7], imaging [8, 9], and sensing [10, 11]

Although the electromagnetic spectrum consists of different regions with interesting properties, terahertz radiation has gained particular interest due to its unique properties and potential for various applications [12–14]. It falls in the frequency range between microwaves and infrared radiation, inheriting some of

the properties of these neighboring regions, and it is capable of penetrating materials that are opaque to visible and infrared light [15]. Promising applications of of terahertz radiation such as security screening [16, 17], medical imaging [18, 19], and communication [20, 21] have been explored among others. However, active, efficient manipulation and control of terahertz radiation still present significant challenges [22].

Another interesting research topic is radiative cooling, a passive cooling approach that utilizes the radiative heat exchange between a surface and the atmosphere to achieve cooling without the need for external power sources [23–26]. Radiative cooling has attracted significant attention due to its potential for energy-efficient cooling in a variety of contexts, including electronic devices [27], and space applications [28]. Despite this increasing interest, achieving efficient and versatile radiative cooling, especially adaptability to changing environmental conditions [29], remains a hot topic of research.

Motivated by the need for advanced materials and techniques that can enable efficient and versatile control over various parts of the electromagnetic spectrum, this thesis presents two different projects that explore the potential of metamaterials in these domains.

1.1.1 Graphene-based metasurface for manipulation of terahertz radiation

Metasurfaces, two-dimensional (2D) metamaterials composed of subwavelength resonators, can be utilized to efficiently tailor an incident electromagnetic wave [30, 31]. They have been used in many applications, such as flat lenses [32, 33], metamirrors [34, 35], polarization converters [36, 37], full-color printers [38], holographs [39, 40], optical vortex generators [41, 42], and beam splitters [43, 44]. Light absorption is another eye-catching characteristics of these artificial systems [45], and metastructures with a nearly perfect light absorption characteristics are referred to as metasurface/metamaterial nearly perfect absorbers (MPAs). In order

to realize nearly perfect light absorption, reflectance is suppressed by matching the effective impedance of the metasurface to that of the incident medium [46]. Simultaneously, transmittance may be eliminated by introducing another metallic film acting as a mirror or by using a similar mechanism in a multilayer system [47]. Based on these approaches, metasurface nearly perfect light absorbers can be categorized as narrowband MPAs [48–54] and broadband MPAs [55–70]. They can also be classified according to their wavelength of operation in the visible [55–58, 71, 72], infrared [59, 73, 74], terahertz (THz) [50–54, 60–69], and microwave ranges [48, 49, 70].

The THz spectrum is referred to as electromagnetic waves ranging from 0.1 to 10 THz that bridges infrared light and microwaves. This range of frequency, which is also called the THz gap, has many important characteristics. Due to their low energy, THz radiations cannot interact with the electrons in atoms. In other words, they do not have the potential to ionize materials, and therefore they cannot damage living tissues. This characteristic makes THz waves very practical for medical imaging and biomedical applications [75]. Moreover, many materials that are opaque to visible light are transparent to THz radiation. This feature makes THz waves practical for scanning passengers in airports [76]. Furthermore, the THz frequencies offer a wide bandwidth in an uncrowded part of the electromagnetic spectrum. Therefore they can be employed for achieving high-rate data transfer in wireless technology [77]. In view of the useful potential applications of THz radiation, progress has been made in THz generation and detection (see, e.g., [78, 79]) as well as in achieving functional metasurfaces for lensing, polarization conversion, splitting, and other applications (see, e.g., [34, 36, 43]). Employing gold-based metasurfaces integrated with semiconductors as active elements has also been introduced as an efficient method to a real-time control and to manipulate THz radiation [80]. Vanadium dioxide (VO_2), which exhibits an insulator-to-metal transition and 3 orders of magnitude in increase in THz electrical conductivity, has also been utilized in realization of active THz metasurfaces [81]. Metasurfaces based on graphene -that is, a low-loss plasmonic material with gate-tunable characteristics- are also the most notable category of active devices for the efficient steering of THz waves [82]. Considering the importance of

light absorbers in THz spectroscopy and communications, on the one hand, and achieving metasurfaces for the active manipulation of THz waves, on the other hand, have recently led researchers to the design and realization of graphene-based metasurfaces for broadband THz light absorption. The first approach for the realization of graphene-based broadband MPAs is to utilize cascaded metasurfaces that are composed of multilayers of patterned graphene surfaces (see, e.g., [67–69]). However, the fabrication and gating of the MPAs in this approach are complex, thereby making it less effective. The second and more effective methodology for the realization of broadband MPAs is to employ appropriately designed metasurfaces based on a single layer of graphene [60–65]. Nevertheless, the reported absorption bandwidths of these metasurfaces are less than 1.5 THz. Recently, a broadband graphene-based MPA has been reported with a bandwidth of almost 3 THz [66], but the patterned graphene sheet is too complex and may not be realized in practice, and that makes the functionality of the suggested device less efficient. Consequently, achieving alternative graphene-based MPAs with doable and less complex designs is still appreciated.

1.1.2 Phase-change-material-based metasurface for adaptive radiative cooling

Every material with non-zero temperature emits electromagnetic radiation with intensities governed by Planck's Law [83]. This thermal radiation is called "black-body radiation" and Stephan-Boltzmann law gives us the emission spectrum of this black-body, where the emission is proportional to the fourth power of the temperature (T^4) and the surface emissivity (ε) [84]. Kirchhoff radiation law states that the emissivity of any surface is also equal to its absorptivity, so the black-body can also be considered a perfect absorber [85].

Managing or manipulating thermal radiation within a specific spectrum range is one of the main approaches to introduce or tackle various applications, including thermal camouflage [86], radiative cooling [87], and energy harvesting [88]. To achieve this aim, metamaterials and their 2D counterparts called metasurfaces,

artificially engineered materials with extraordinary electrical, optical, and thermal properties, are utilized. Metamaterials are promising candidates for proposing novel devices that can manage and manipulate thermal radiation within a specific spectrum. These artificial materials with various geometrical shapes such as gratings [89], crosses [90], hole-arrays [91], or planar [92] are exploited to achieve strong light-matter interactions in terahertz [93], near-infrared [94], and mid-infrared [95] regimes.

Despite these broad applications of metamaterial-based designs ranging from superlenses [96] to antennas [97], their geometry-dependent spectral responses cannot be controlled in real-time. In recent studies, phase-change materials (PCMs) such as vanadium dioxide (VO_2) [98] and germanium antimony telluride ($Ge_3Sb_2Te_6$) [99, 100] gained lots of interest among researchers to add tunability of the spectral response to the metamaterial structures. For example, Osgouei et al. demonstrated the switchable narrowband to broadband absorption response by incorporating a VO_2 layer in a Si grating structure [101]. PCMs change their crystal structure with respect to their temperature which in turn changes their optical responses. Samarium nickelate ($SmNiO_3$) is one of these materials exhibiting dielectric characteristics at 25 °C and metallic characteristics at 140 °C. This feature allows researchers to design thermally tunable devices by incorporating a PCM layer in the structures [102–104].

1.2 Thesis Outline

In Chapter 2, the numerical investigation of a tunable graphene-based metasurface absorber for the active and broadband manipulation of terahertz radiation was presented. In this study, we propose a metasurface whose optical response can be tuned by applying an external voltage. The design enables the control of the absorption over a 3 THz bandwidth which was the record at the time of publication.

In Chapter 3, we propose an inverse pyramid grating metasurface consisting of a phase-change-material that allows a thermally tunable radiative cooling with angle insensitivity. Samarium nickelate ($SmNiO_3$) was utilized so that the absorption/ emission peak of the design shifts from 8.08 μm to 9.26 μm when the temperature of the structure changes from 25°C to 140°C.

Finally, in chapter 5, we present the conclusion of the thesis, future outlook and possible 5G and beyond applications.

Chapter 2

Graphene-based Metasurface absorber for the Active and Broadband Manipulation of Terahertz Radiaton

This chapter is on part reprinted with permission from: **Ekin Bircan Boşdurmaz**, Hodjat Hajian, Veysel Erçağlar, and Ekmel Özbay, Journal of the Optical Society of America B, vol. 38, no. 9. The Optical Society, p. C160, Aug. 10, 2021. doi: 10.1364/josab.427975.

2.1 Introduction

In this chapter, we design and propose a novel graphene-based MPA with broadband, polarization-insensitive, and omnidirectional characteristics. The graphene-based MPA comprises a single layer of graphene square patches with two different dimensions that are separated from an optically thick Au bottom reflector with an SiO_2 spacer layer. The suggested MPA is capable of absorbing THz radiation within a bandwidth of almost 3 THz, for which the numerically obtained absorption response of the MPA is verified by analytical calculations. The spectral location of the broad bandwidth can be either actively tuned by modifying the chemical potential of graphene or passively amended by changing the geometrical parameters. Moreover, owing to the simplicity of its design, the proposed MPA can be realized in practice. It is expected that this simple and novel design will find potential applications in THz spectroscopy and communications.

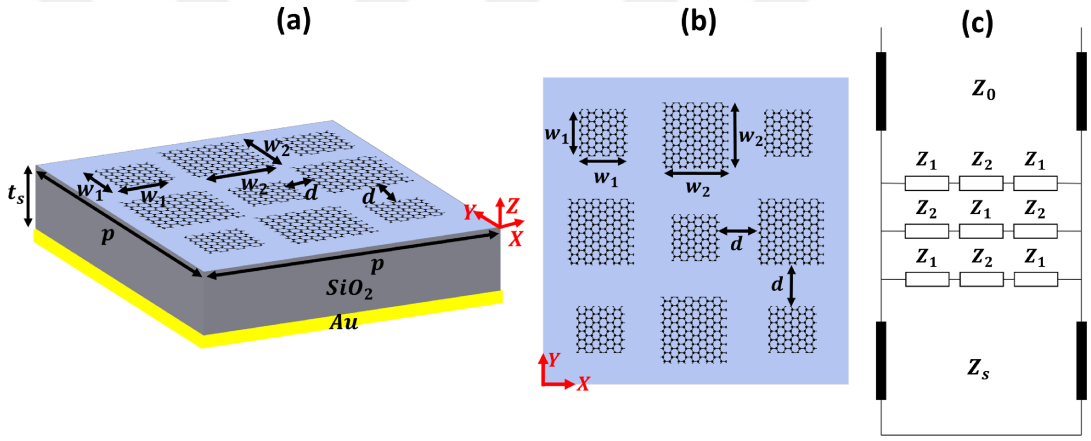

Figure 2.1: (a) and (b) Perspective and top-view schematics of the unit cell of the graphene-based MPA, respectively. As shown, in this arrangement, the unit cell comprises an array of two graphene patches of widhts w_1 and w_2 that are detached by a gap of width d, and $p_x = p_y = 3\left(\frac{w_1+w_2}{w} + d\right)$. As seen, the top graphene patches are separated from the optically thick Au mirror by an SiO_2 spacing layer with the thickness t_s. (c) Equivalent circuit model for the proposed absorber. In this model Z_1 and Z_2 stand for the impedances of w_1 and w_2 graphene patches, and Z_0 and Z_1 refer to the impedances of air and the spacing layer, respectively.

2.2 Analytical Modeling

In this section, we provide an analytical approach for the investigation of the absorption of the graphene-based MPA based on an equivalent circuit model. Using this approach, we can evaluate and analyze our numerical results (see Section 2.3) that are obtained by finite-difference time-domain (FDTD) simulations [105].

The perspective and top-view schematics of a unit cell of the graphene-based MPA are illustrated in panels (a) and (b) of Fig 2.1. As seen from these panels, each unit cell with periodicity $p_x = p_y$ comprises an array of square patches of widths w_1 and w_2 [with gaps d between them in away that $p_x = p_y = 3\left(\frac{w_1+w_2}{2} + d\right)$] and separated from an optically thick Au mirror by an SiO_2 spacer layer of width t_s. According to the configuration of the patches, the equivalent circuit model of the proposed MPA is presented in Fig. 2.1(c). In this model, each graphene patch is described by an impedance as [52]:

$$Z_{1,2} = \left(\frac{p_x}{3w_{1,2}}\right)^2 \left(\frac{1}{\sigma_g} - \frac{n_{1,2}}{i\omega\varepsilon_{eff}}\right) \Big/ m_{1,2} \tag{2.1}$$

Here n and m are fitting parameters, $\varepsilon_{eff} = \varepsilon_0(1 + n^2_{\mathrm{SiO_2}})/2$, and $\sigma_g = \sigma_g^{\mathrm{intra}} + \sigma_g^{\mathrm{inter}}$ is the optical conductivity of graphene, which is a function of frequency and temperature and can be formulated as [106]:

$$\sigma_g^{\mathrm{intra}}(\omega, T) = \frac{e^2}{4\hbar}\frac{i}{2\pi}\left\{\frac{16k_BT}{\hbar\Omega}\ln\left(2\cosh\left(\frac{\mu}{2k_BT}\right)\right)\right\}, \tag{2.2a}$$

$$\begin{aligned}\sigma_g^{\mathrm{inter}}(\omega, T) =& \frac{e^2}{4\hbar}\left\{\frac{1}{2} + \frac{1}{\pi}\arctan\left(\frac{\hbar\Omega - 2\mu}{2k_BT}\right)\right. \\ &\left. - \frac{i}{2\pi}\ln\left(\frac{(\hbar\Omega + 2\mu)^2}{(\hbar\Omega - 2\mu)^2 + (2k_BT)^2}\right)\right\},\end{aligned} \tag{2.2b}$$

with $\Omega = \omega + i\tau^{-1}$, e is the electron charge, k_B is the Boltzmann constant, τ is the electron relaxation time, and $\hbar$ is the Planck constant over 2π. Consequently,

the total effective impedance of the top patches is written as

$$Z_{eff} = \frac{(Z_1 + Z_2/2)(Z_1 + 2Z_2)}{2Z_1 + 5Z_2/2} \tag{2.3}$$

As a result, the input impedance can be calculated as

$$Z_{in} = \frac{Z_{eff} Z_s}{i \cot\left(\frac{n_s \omega}{c} t_s\right) Z_{eff} + Z_s} \tag{2.4}$$

and the reflection (R) of light from the MPA is given by

$$R = |(Z_{in} - Z_0)/(Z_{in} + Z_0)|^2. \tag{2.5}$$

Here c is the speed of light, $Z_s = Z_0/n_s$, $n_s = n_{\mathrm{SiO_2}}$, and Z_0 is the free-space impedance. Note that, due to the presence of the optically thick bottom gold layer, light transmission through the metasurface is zero, and therefore the absorption of light is calculated as $A = 1 - R$. In Figs. 2.3(a) and 2.3(b) , we compare the analytical results calculated from Eqs. 2.4 and 2.4 with the ones obtained numerically. Note that, in our calculations in this paper, $\tau = 0.1$ ps, $w_1 = 3\ \mu m$, $w_2 = 4\ \mu m$, and the refractive index data of SiO_2 is chosen according to Ref. [107] . It is noteworthy that, in the THz range, the optical conductivity of a multilayer graphene that is composed of N_g layers can be expressed as $\frac{N_g i e^2 \mu}{\pi \hbar^2 (\omega + i\tau^{-1})}$. Consequently, at the same frequency and with an equal value of τ, graphene-based metasurfaces with identical values of $N_g \mu$ are expected to exhibit similar optical responses. In other words, a metasurface based on a single layer graphene with $\mu = 1$ eV acts as a bilayer graphene-based metasurface with $\mu = 0.5$ eV.

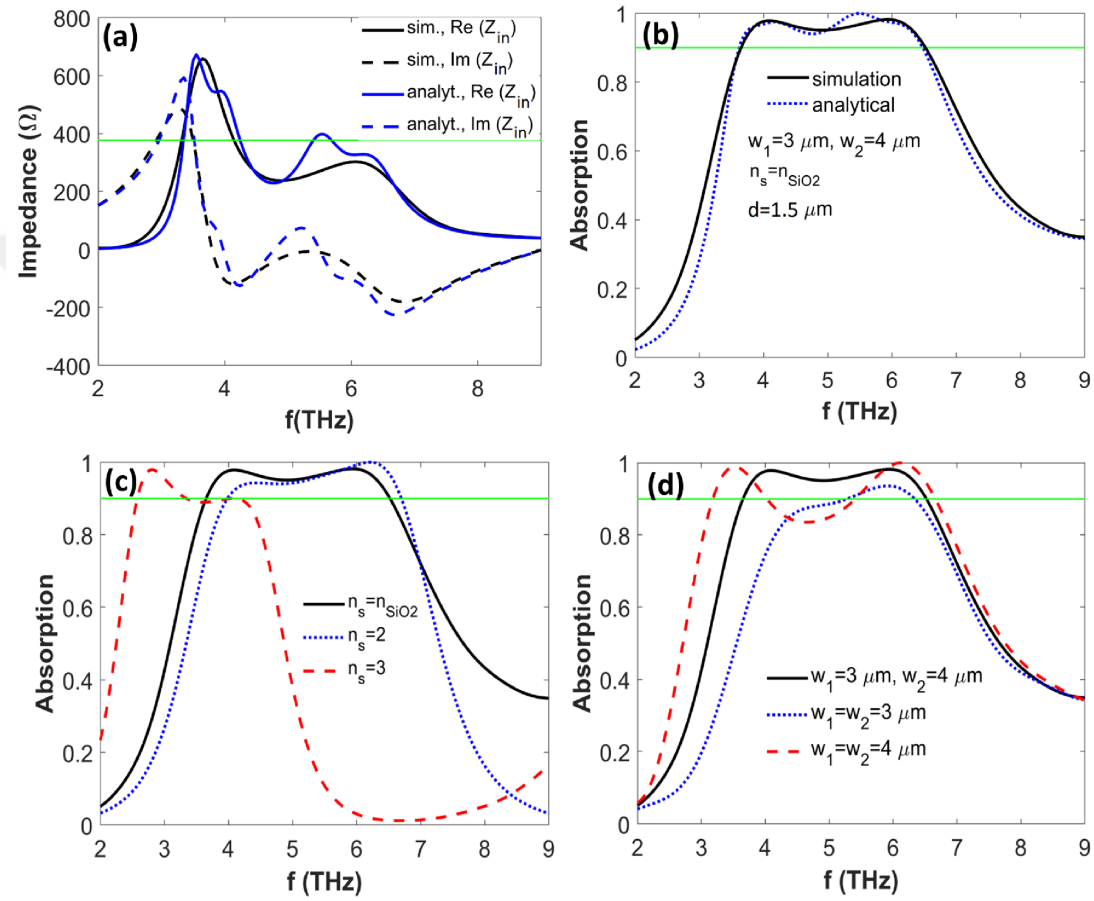

Figure 2.2: (a) Analytically (blue curves) and numerically (black curves) obtained input impedances of the graphene-based MPA. Solid green curve indicates $Z_0 = 120\pi$. (b) Dotted blue and solid black curves illustrate the analytically and numerically obtained absorption of the MPA for normal incident light, respectively. The optimized values of the geometrical parameters (d and t_s) are also highlighted in this panel. (c) Absorption of the MPA for the different values of n_s, while the geometrical parameters are kept as in panel (b). In panel (d), absorption of the MPA (solid black curve) is compared to the cases for which the widths of the patches are equal as 3 μm (dotted blue curve) and 4 μm (dashed red curve). Note that, that in panels (b)-(d), the solid green line indicates $A = 90\%$ and for all of the results in this figure $\mu = 1$ eV. The solid black curves in these panels are the same.

2.3 Results and Discussions

In Figs. 2.2(a) and 2.2(b) , we provide the numerically obtained results for the broadband graphene-based MPA and compared them with the analytical calculations. For the MPA shown in Figs. 2.1(a) and 2.1(b), at $\mu = 1$ eV, the analytically calculated input impedance that is based on Eq. 2.4 for $n_{1,2} = (0.377, 0.446)$ and $m_{1,2} = (2.721, 0.418)$ is compared to the numerically obtained one in Fig. 2.2(a). As seen, there is an acceptable agreement between the real and the imaginary parts of the analytical and numerical impedances. This agreement leas to the match between the analytically calculated absorption spectrum based on Eq.2.5 [dotted blue] and the numerically calculated one shown in the solid black curve in Fig. According to this figure, the broadband absorption region extends from $f = 3.64$ THz to $f = 6.55$ THz; i.e., an almost 3 THz absorption bandwidth is obtained. According to Palik's data [108], SiO_2 is a lowly dispersive material in the THz region, where $1.96 < \Re(n_s) < 2.2$ and $0.01 < \Im(n_s) < 0.065$. Taking $n_s = 2$ as a hypothetical material for the spacer layer for which the refractive index is close to n_{SiO_2}, it is observed that the broadband absorption regions is blueshifted and slightly narrowed, as the dotted blue and solid black curves in Fig. 2.2(c) are compared. On the other hand, the dashed red curve in this figure proves that by increasing the refractive index of the spacer layer to a larger hypothetical value (i.e., $n_s = 3$), the broadband response of the MPA is totally distorted and a narrowband response at lower frequencies is achieved. It is also observed from Fig. 2.2(d) that once all the patches of the MPA have the same dimensions with $w_1 = w_2 = 3\ \mu m$ (dotted blue curve) or $w_1 = w_2 = 4\ \mu m$ (dashed red curve), the broadband absorption response of the MPA is transferred to a narrowband one with a single resonance or one with two resonances, respectively.

To understand the physical mechanism behind the broadband response of the proposed MPA, in Fig. 2.3, we examine the electric and magnetic field profiles at the two peaks ($f = 4.1$ THz and 5.86 THz) and the deep ($f = 4.83$ THz) in the nearly perfect and broadband absorption region of the solid black curve of Fig. 2.2(b).

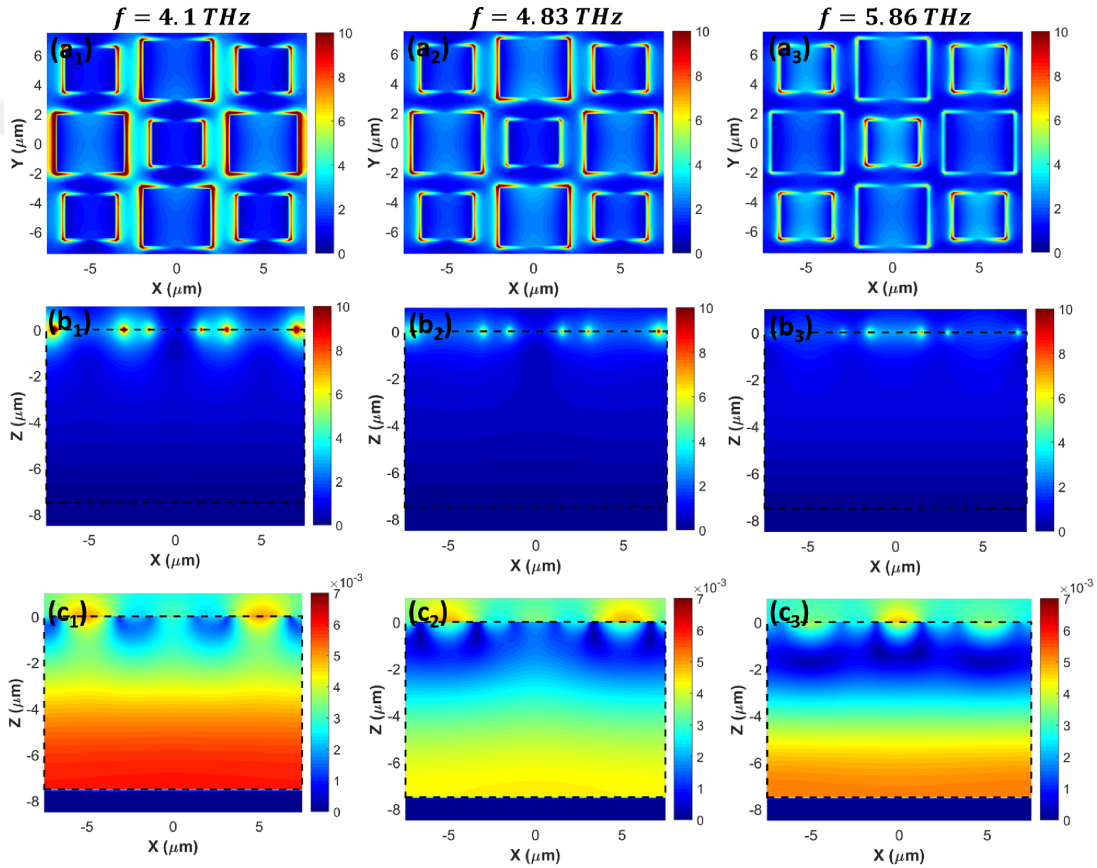

Figure 2.3: Panels (a_i), (b_i), and (c_i) $[i = 1, 2, 3]$, respectively, illustrate the normalized values of the top view of $|\mathbf{E}|$, side view of $|\mathbf{E}|$, and side view of $|\mathbf{H}|$ at the two peaks ($f = 4.1$ THz and 5.86 THz) and the deep ($f = 4.83$ THz) in the nearly perfect and broadband absorption bandwidth of the solid black curve of Fig. 2.2(a). The dashed rectangle in panels (b_i), and (c_i) indicates the SiO_2 spacer layer.

The top-view $|\mathbf{E}|$ mode profiles of the resonant peaks of absorption at $f = 4.1$ THz and 5.86 THz are shown in panels (a_1) and (a_3) of Fig. 2.3. It is seen from these panels that, at $f = 4.1$ THz, the larger graphene patches (w_2 patches) are strongly excited, while 5.86 THz, the smaller patches (w_1 patches) are mostly excited. On the other hand, at $f = 4.83$ THz, that corresponds to the deep in the broadband absorption region of Fig. 2.2(b), in which both w_1 and w_2 graphene patches are almost equally responsible for the plasmonic excitation of the MPA as seen in Fig. 2.3(a_2) In agreement with the top-view mode profiles, the side-view of $|\mathbf{E}|$, which is depicted in Figs. refch2fig3(b_1)-2.3(b_3), shows that those plasmonic excitations are strongly bound to the graphene patches. This is in agreement with the highly localized THz surface plasmon polaritons supported by a sheet of graphene. From the side view of $|\mathbf{H}|$ at those frequencies, it is obvious that the magnetic field is not only strongly enhanced between the graphene patches, but it also has as strong interaction with the bottom Au mirror and is confined beneath the patches in the spacer layer as seen in Figs. 2.3(c_1)-2.3(c_3). This observation reveals that the propagating surface plasmon resonances supported by graphene-based MPA are responsible for the broadband absorption response. It should be noted that changes in the thickness of the spacer layer considerably affect the nearly perfect absorption response of the MPA (see Fig. 2.4)

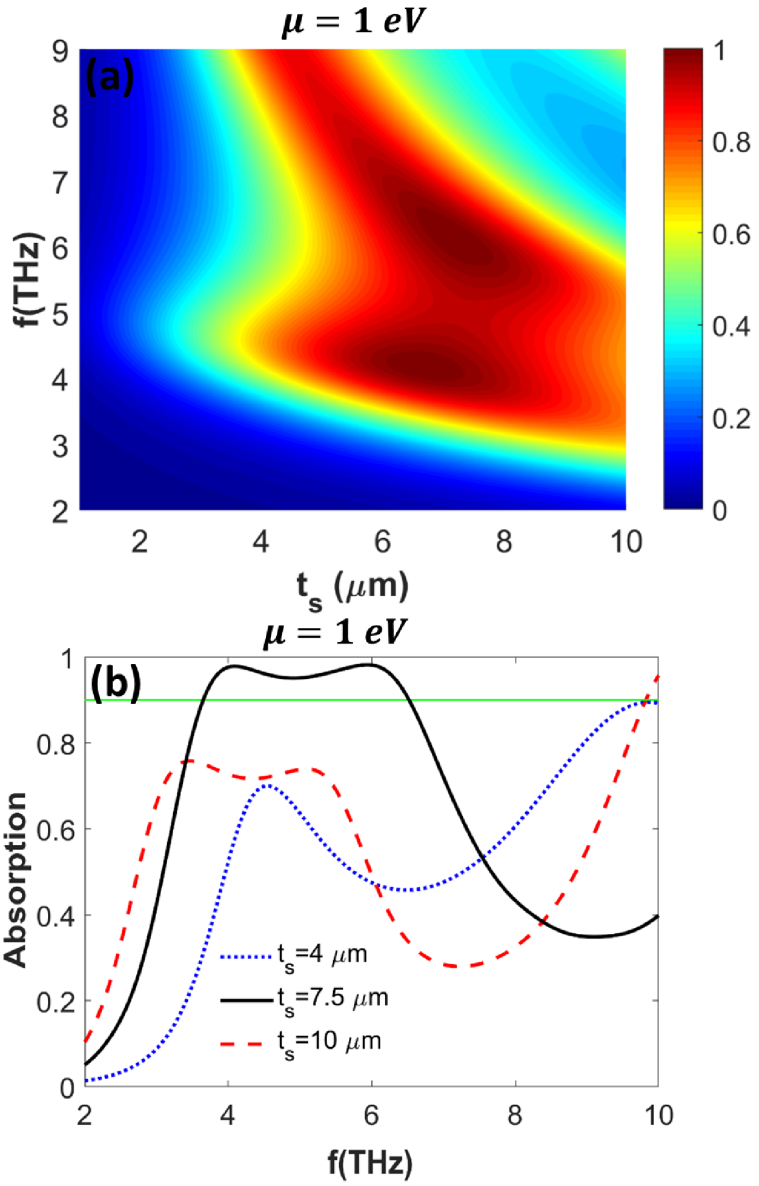

Figure 2.4: (a) Absorption of the graphene-based MPA as a function of the thickness of the spacer layer (t_s). (b) Similar to panel (a), while the absorption values are depicted for the three values of t_s, i.e., $t_s = 4\ \mu m$ (dotted blue curve), $t_s = 7.5\ \mu m$ (solid black curve; the optimized result discussed in Fig. 2.2), and $t_s = 10\ \mu m$ (dashed red curve). Note that, the results are obtained for the design shown in Fig. 2.1(a) with $d = 1.5\ \mu m$ and $\mu = 1$ eV.

Taking $d = 1.5\ \mu m$ and $\mu = 1$ eV in the calculations, the absorption spectrum of the MPA for the different values of the thickness of the spacing SiO_2 layer are shown in Fig.2.4(a). In agreement with this figure, Fig.2.4(b) represents the absorption of the MPA for three values of the thickness of the spacer layer; i.e., $t_s = 4\ \mu m$ (dotted blue curve), $t_s = 7.5\ \mu m$ (solid black curve), and $t_s = 10\ \mu m$ (dashed red curve). It is clear from Fig. 2.4 that changes in the thickness of the spacer layer significantly modify the absorption response. In other words, at the optimized value of t_s (i.e., $t_s = 7.5\ \mu m$), the broadband response is observed, while by decreasing/increasing this thickness, it is possible to achieve two/one distinct narrow resonance(s). For example, as seen from the dotted blue curve in Fig. 2.4(b), two strong absorptive resonances are achieved at $f = 4.53$ THz and $f = 9.82$ THz.

One of practically important characteristics of the MPAs is the dependency of their absorption response to the polarization and angle of incident light. This feature is examined in Fig. 2.5.

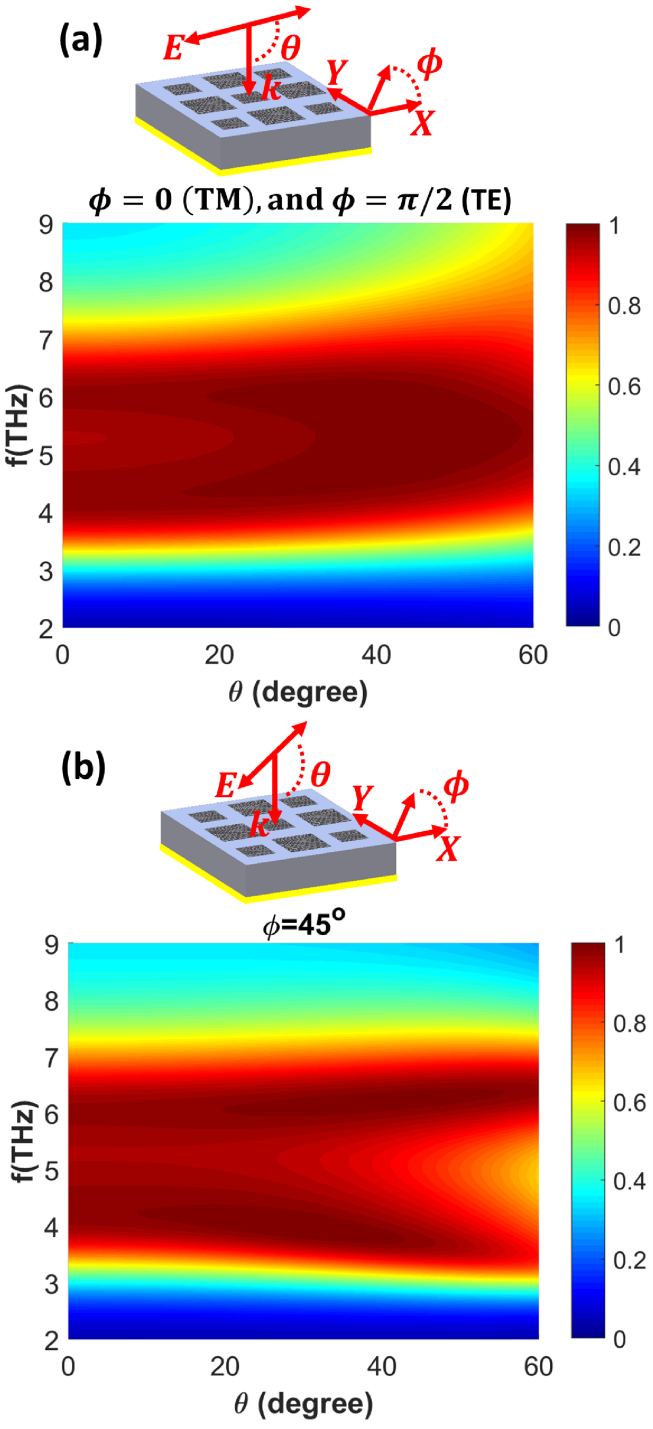

Figure 2.5: Dependence of the absorption spectra of the MPA on the angle of incidence θ for three different values of the azimuthal angle ϕ; i.e., (a) $\phi = 0, \pi/2$ and (b) $\phi = 45^\circ$

Fig. 2.5(a) illustrates the dependency of the absorption spectra of the MPA for the x-polarized or TM ($\phi = 0$) and y-polarized or TE ($\phi = \pi/2$) incident light. Here, the azimuthal angle ϕ denotes the in-plane direction of the electric field with respect to the x and y axes. It is seen from this figure that the nearly perfect absorptive response of the graphene-based MPA is kept unchanged up to $\theta = 50^\circ$ while the bandwidth of the spectrum is shrunk for larger incident angles. For the case that the azimuthal angle is chosen as $\phi = 45^\circ$, the absorption response of the MPA also remains as broad as the normal incidence illumination up to $\theta = 45^\circ$, but for the larger angles of incidence, two narrowband perfect absorption peaks are achieved as shown in Fig. 2.5(b). Consequently the designed graphene-based metasurface can act as a broadband, polarization-insensitive, and omnidirectional MPA up to $\theta = 45^\circ$, thereby meeting the needs for practical applications.

Taking $d = 1.5\ \mu m$ and $\mu = 1$ eV, we have designed a graphene-based MPA to achieve a THz broadband absorption response with the absorption bandwidth of almost 3 THz. In Fig. 2.6, we examine how the absorptive response of the MPA can be actively tuned via changes in the chemical potential of graphene.

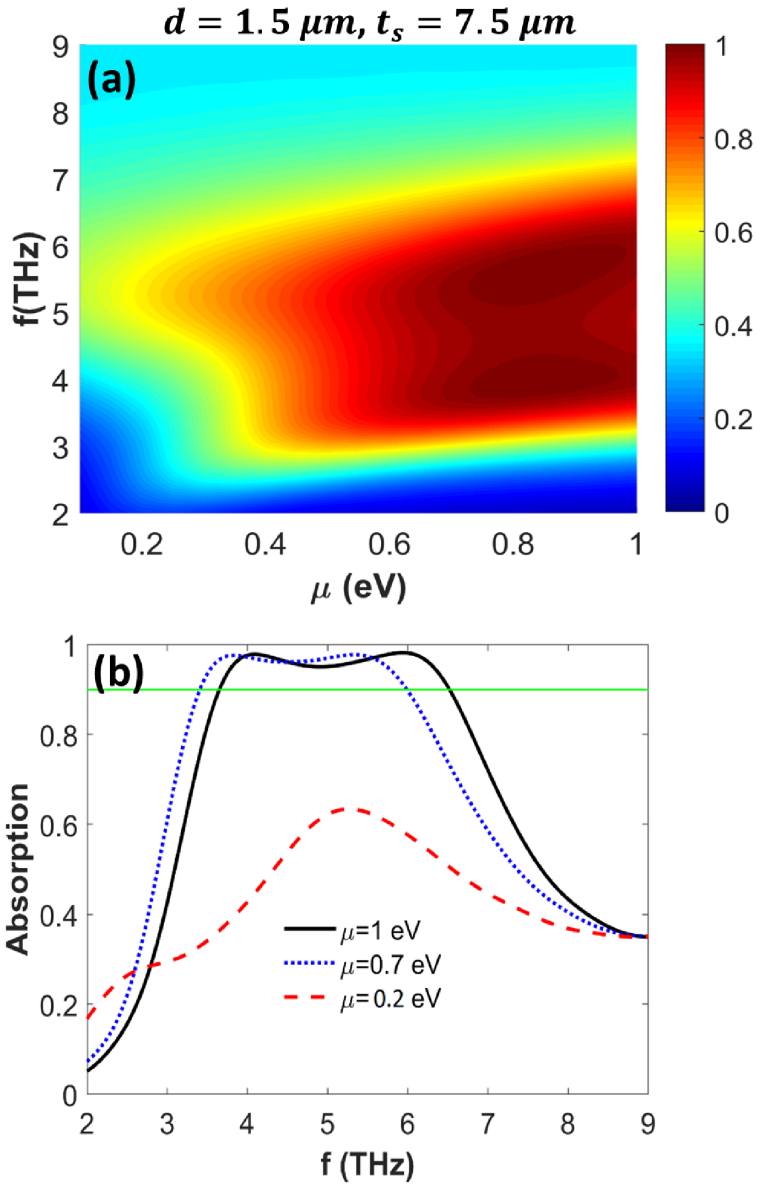

Figure 2.6: (a) Absorption spectra of the MPA as a function of the chemical potential of graphene for $d = 1.5\ \mu m$ and $t_s = 7.5\ \mu m$. In agreement with panel (a), (b) illustrates the absorption response for $\mu = 1$ eV (solid black curve), $\mu = 0.7$ eV (dotted blue curve), and $\mu = 0.5$ eV 2.6 (dotted red curve). The solid green line indicates $A = 0.9$ and the results are obtained at normal incidence.

It is seen in Fig. 2.6(a) that, for $d = 1.5\ \mu m$, the MPA response can be noticeably tuned from a narrowband absorption at low values of the chemical potential of the graphene [e.g., $A = 64\%$ at $f = 5.26$ THz and $\mu = 0.2$ eV; see the dashed red curve in Fig. 2.6(b)] to a broadband one at $\mu > 0.60$ eV. Moreover, the broadband absorption bandwidth is also blueshifted and widened by increasing the chemical potential of graphene, as the dotted blue curve ($\mu = 0.7$ eV) in Fig. 2.5(b) is compared to the solid black one ($\mu = 1$ eV). In other words, the spectral tuning of the bandwidth is achieved. Note that the bandwidth for the $\mu = 0.7$ eV case in Fig. 2.5(b) is 2.6 THz (located at 3.4 to 6 THz).

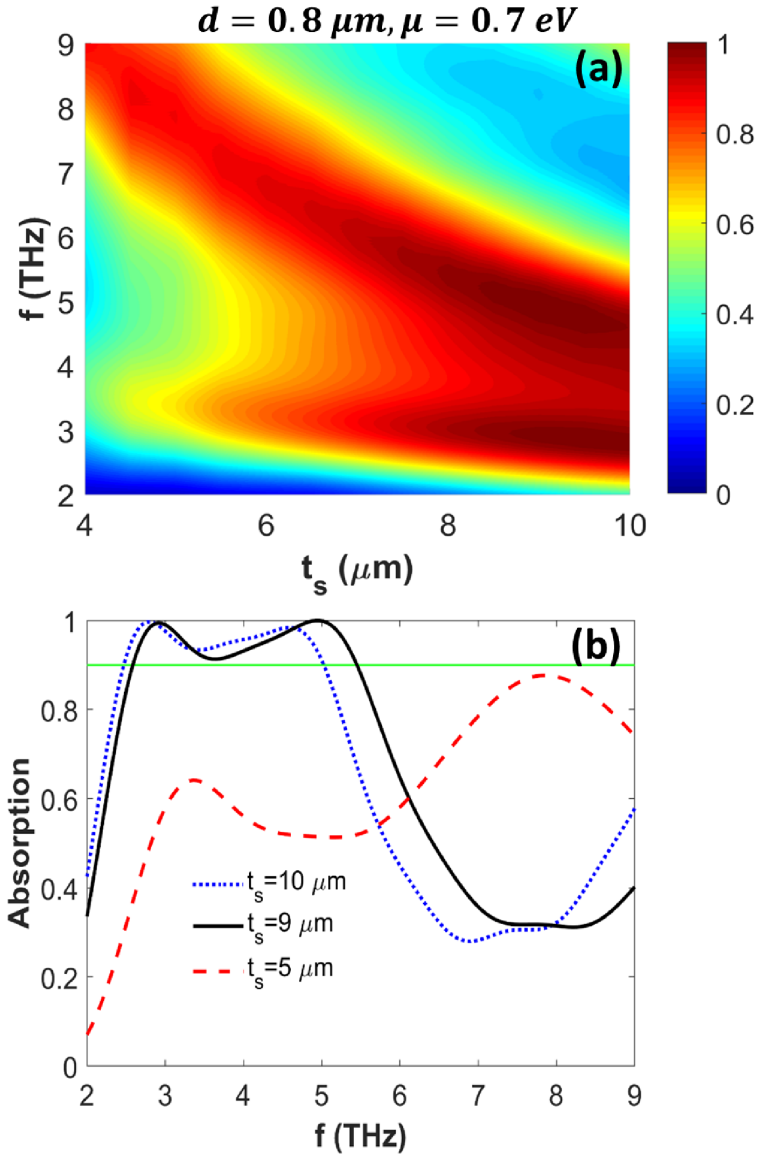

Figure 2.7: (a) illustrates the dependency of the MPA's absorption spectrum for $d = 0.8\ \mu m$ and $\mu = 0.7$ eV on the spacer layer thickness. (b) Results of panel (a) for three different values of t_s, i.e., $t_s = 7.5\ \mu m$ (dotted blue curve), $t_s = 9\ \mu m$ (solid black curve), and $t_s = 5\ \mu m$ (dashed red curve). The results are obtained at normal incidence and the solid green line highlights $A = 0.9$. Note that, for this design, the locations of the w_1 and w_2 patches that are shown in Fig. 2.1 (a) are interchanged, i.e., there are five (four) w_2 (w_1) patches in the unit cell.

However, from a practical point of view, obtaining a broadband absorption with 3 THz bandwidth may be more desirable for $\mu < 1$ eV, e.g., obtaining 0.7 eV may be more feasible in practice for the chemical potential of graphene. To this end, taking $\mu = 0.7$ eV and decreasing d from 1.5 to 0.8 μm, the absorption spectrum of the MPA as a function of the thickness of the SiO_2 layer is examined in Fig. 2.7(a). It is clearly observed in this figure that for smaller values of t_s, the metasurface exhibits narrowband responses, e.g., for $t_s = 5$ μm, two strong absorption resonances ($A > 60\%$) are obtained at $f = 3.35$ THz and $f = 7.86$ THz as seen from the dashed red curve in Fig. 2.7(b). On the other hand, by increasing t_s, the graphene-based metasurface acts as a broadband MPA and represents a bandwidth of almost 3 THz at $t_s = 9$ μm for the case of $\mu = 0.7$ eV as seen from the solid black curve in Fig. 2.7(b). Note that, in this study, we have introduced two designs with broadband responses (bandwidth 3 THz) in Fig. 2.2and Fig. 2.7. The results of Fig.2.2 are obtained at $\mu = 1$ eV, while for the results of Fig.2.7, the value of the chemical potential of graphene is taken as $\mu = 0.7$ eV. From a practical point of view, $\mu = 0.7$ eV is expected to be achieved by top-gating in the experiment (see Ref. [108]). However, as we explained in Section 2.2 and according to FDTD simulations, since $N_g\mu$ affects the response of our designs, the results of Fig.2.2 and Fig. 2.7 are exactly identical responses of the metasurfaces based on bilayer graphene with $\mu = 0.5$ eV and $\mu = 0.35$ eV, respectively, that can be achieved by top-gating [108]. As the last point, it is worth investigating the relative absorption bandwidth of the suggested metasurface absorbers that is expressed as the ratio of the bandwidth to the frequency; i.e., $W_B = 2 \times \frac{f_{max}-f_{min}}{f_{max}+f_{min}} \times 100\%$, where f_{max} and f_{min} denote the maximum and minimum frequencies in the nearly perfect absorption region with $A > 90\%$. For the broadband absorbers, the relative absorption bandwidth is expected to be $> 50\%$. For the solid black curve shown in Fig. 2.2(b), the calculated value of the absorption bandwidth is almost 58%, and for the solid black curve in Fig. 2.7(b), we have $W_B \approx 72\%$.

Chapter 3

Adaptive Thermally Tunable Radiative Cooling with Angle Insensitivity Using Phase-Change-Material-Based Metasurface

3.1 Introduction

In this chapter, we proposed an adaptive metamaterial-based absorber using $SmNiO_3$ inverse pyramid gratings on top of a silver (Ag) reflector, which exhibits broadband perfect absorption on the mid-infrared (MIR) regime. The absorption spectrum of the design is thermally tunable due to the phase variation of the utilized $SmNiO_3$ pyramids from metallic to insulator phases. This tunability in the position of the resonance peak with the simplicity of the structure makes the design more practical than the previous studies. The optical response of the proposed design is studied using a commercial finite-difference-time-domain software package [109] and the design's angle insensitivity is investigated simulations from zero up to 60° for both transverse magnetic (TM) and transverse electric (TE) polarizations which is given in Fig.3.4(b). In addition, the structural parameters of the design are optimized for radiative cooling performance and the effect of geometrical parameters on the performance of the design are investigated.

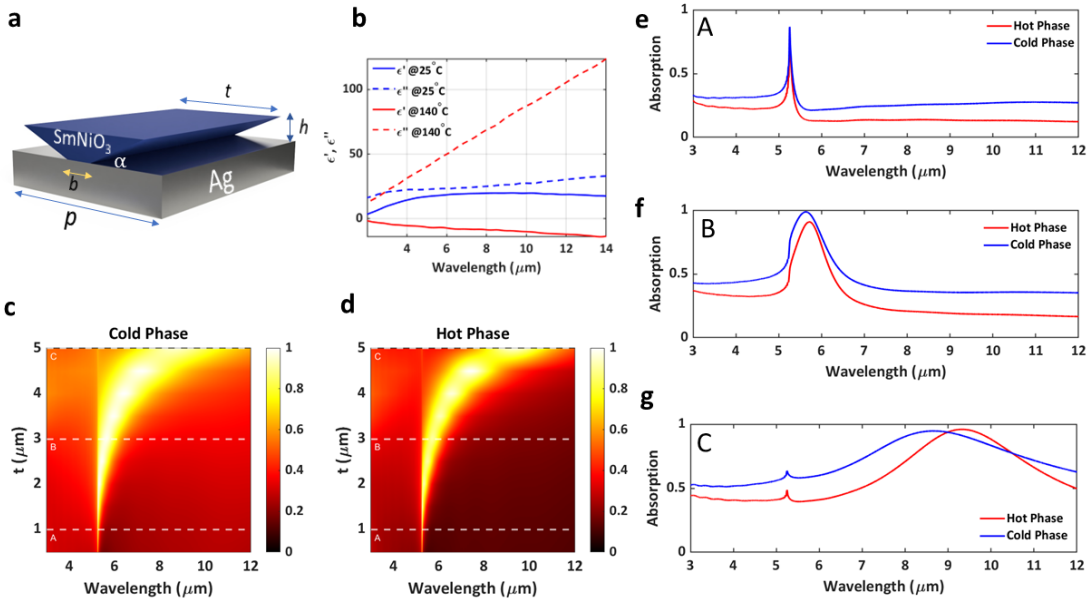

Figure 3.1: (a) Schematic illustration of the designed metasurface. (b) Real and imaginary parts of permittivity of $SmNiO_3$ at 25° C and 140° C. (c)-(d) Absorption of the structures with $\boldsymbol{t} = 1\ \mu m$, $\boldsymbol{t} = 3\ \mu m$, and $\boldsymbol{t} = 5\ \mu m$ at 25° C - 140° C ($\boldsymbol{p} = 5250\ nm$, $\boldsymbol{h} = 750\ nm$, $\boldsymbol{b} = 500\ nm$)

3.2 Results and Discussion

A schematic representation of the proposed design in Fig.3.1(a), in which $SmNiO_3$-based inverse pyramid gratings are placed on top of an Ag bottom reflector. The optical constants of the bottom reflector (Ag) are extracted from the CRC Handbook of Chemistry and Physics [110], whereas the real and imaginary components of the permittivity of $SmNiO_3$ for both cold (25 °C) and hot (140 °C) states are given in Fig.3.1(b) [111]. The dimensions of the inverse pyramid gratings are denoted with t, b, h, and p, corresponding to the top and bottom width, height, and period of the grating, respectively. A commercial finite-difference time-domain (FDTD) simulation software (Lumerical FDTD Solutions) is utilized to compute the optical response of the proposed metasurface-based absorber and investigate the effects of the geometrical parameters on the optical response [109]. The simulations were carried out in a 2D geometry due to the periodicity of the structure in the z plane. A plane wave source propagating along the y-axis is utilized to illuminate the structure from the $SmNiO_3$ side. Periodic boundary conditions are utilized in the x direction and perfectly matched layers are utilized in the y direction. A reflection monitor which is placed behind the source is used to collect the reflected wave from the surface, whereas a transmission monitor is used after the Ag layer to collect any transmitted wave.

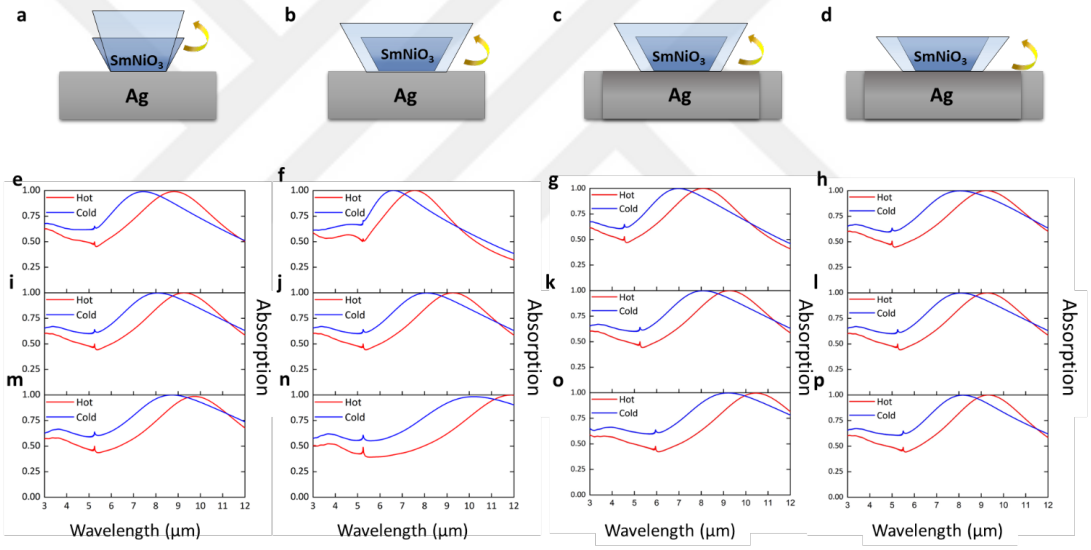

Figure 3.2: (a)-(d) Schematic representation of the scalings with the respective rules from the optimal design. (e)-(h) Absorption spectra of the down-scaled structures. (i)-(l) Absorption spectra of the optimal design. (m)-(p) Absorption spectra of the up-scaled structures.

Radiative cooling is a process of dumping thermal energy into outer space instead of the environment, which requires the resonance peak of the absorption spectrum of the proposed metasurface-based design to be placed in the transparency window of the atmosphere. The bottom Ag reflector is optically thick enough to eliminate the transmission from the structure leading to the dependency of the absorbance to the reflectance. In the proposed structure, the peak positions of the absorption spectrum are a function of the periodicity ($\boldsymbol{p}$), height ($\boldsymbol{h}$), and width (top ($\boldsymbol{t}$) and bottom ($\boldsymbol{b}$)) of the structure. Additionally geometrical parameters of angle ($\boldsymbol{\alpha = atan\frac{2h}{t-b}}$) and filling ratio ($\boldsymbol{FR = \frac{t}{p}}$) are defined in the design of the grating leading to inverse pyramid grating when $\boldsymbol{\alpha < 90°}$ ($\boldsymbol{b < t}$), rectangular grating when $\boldsymbol{\alpha = 90°}$ ($\boldsymbol{b = t}$), and pyramid grating when $\boldsymbol{\alpha > 90°}$ ($\boldsymbol{b > t}$). Therefore, three different structures can be considered in the probable design of a tunable nanoantenna emitter by the variation of temperature. Variation in absorptivity of a typical design versus the pyramid angle is investigated by fixing $\boldsymbol{p}$, $\boldsymbol{h}$, and $\boldsymbol{b}$ at **5250** nm, **750** nm, and **3000** nm, respectively, while $\boldsymbol{t}$ is varied between **500** nm to **5000** nm. The results given in Fig. 3.1(c) and (d) at different temperatures (cold and hot states) demonstrate that only the inverse pyramid has a tunable spectral response versus temperature changes since the distance between the edges and the bottom reflector is increasing towards the top corner of the pyramid which allows the design to support multiple modes. So the optimized design should have $\boldsymbol{t > b}$ for effective radiative cooling. This conclusion can be better visualized by presenting absorption responses at three different thicknesses (1 μm, 3 μm, and 5 μm) given in Fig.3.1(e)-(g). It is seen that decreasing the angle broadens the absorption responses at both cold and hot states while heating the metasurface can cause redshift at smaller angles. In the first case where $\boldsymbol{t < b}$, the structure resembles a pyramid. According to the absorption spectra given in Fig.3.1(e), it can be seen that the structure supports a narrow resonance located at 5.25 μm both at the cold and hot phases. Although the magnitude of the absorption changes between cold and hot phases, the peak location does not change which makes this design non-adaptive. On the second case, the structure with $\boldsymbol{t = b}$ corresponding to a rectangular grating is investigated. Fig.3.1(f), shows the absorption spectra, where the resonance

occurs at **5.63** μm and **5.71** μm for the cold and hot phases, respectively. Although the grating structure has broader resonances than the pyramid structure, the resonance shift between the cold and hot phases is not enough to provide a good adaptive radiative cooling. Finally, the case with $\boldsymbol{t > b}$ was investigated. This design was named as inverse pyramid and it has wide resonance peaks occurring at **8.65** μm and **9.32** μm for cold and hot phases respectively as shown in Fig.3.1(g).

Due to the thermally tunable capability of inverse pyramid design caused by the phase transition from the cold state to the hot state, the geometrical parameters are optimized for radiative cooling applications. Therefore, the optimal dimensions are found to be $\boldsymbol{t = 4.2}$ μm, $\boldsymbol{b = 0.8}$ μm, $\boldsymbol{h = 750}$ nm, and $\boldsymbol{p = 5250}$ nm. The optimized design has resonance peaks occurring at **8.08** μm and **9.26** μm for the cold and the hot phases respectively which can be seen in 3.2 (i) - (l).

For the first set of simulations, as given in the first column of Fig.3.2, the height of the structure, $\boldsymbol{h}$, is varied between **650** nm to **850** nm while keeping the $\boldsymbol{t}$, $\boldsymbol{b}$, and $\boldsymbol{p}$ constant. In this case, the resonance peaks for both cold and hot phases redshift with the increasing $\boldsymbol{h}$, since the increase in $\boldsymbol{h}$ effectively increases the length of the cavity formed by the sides of the inverse pyramid and the bottom reflector.

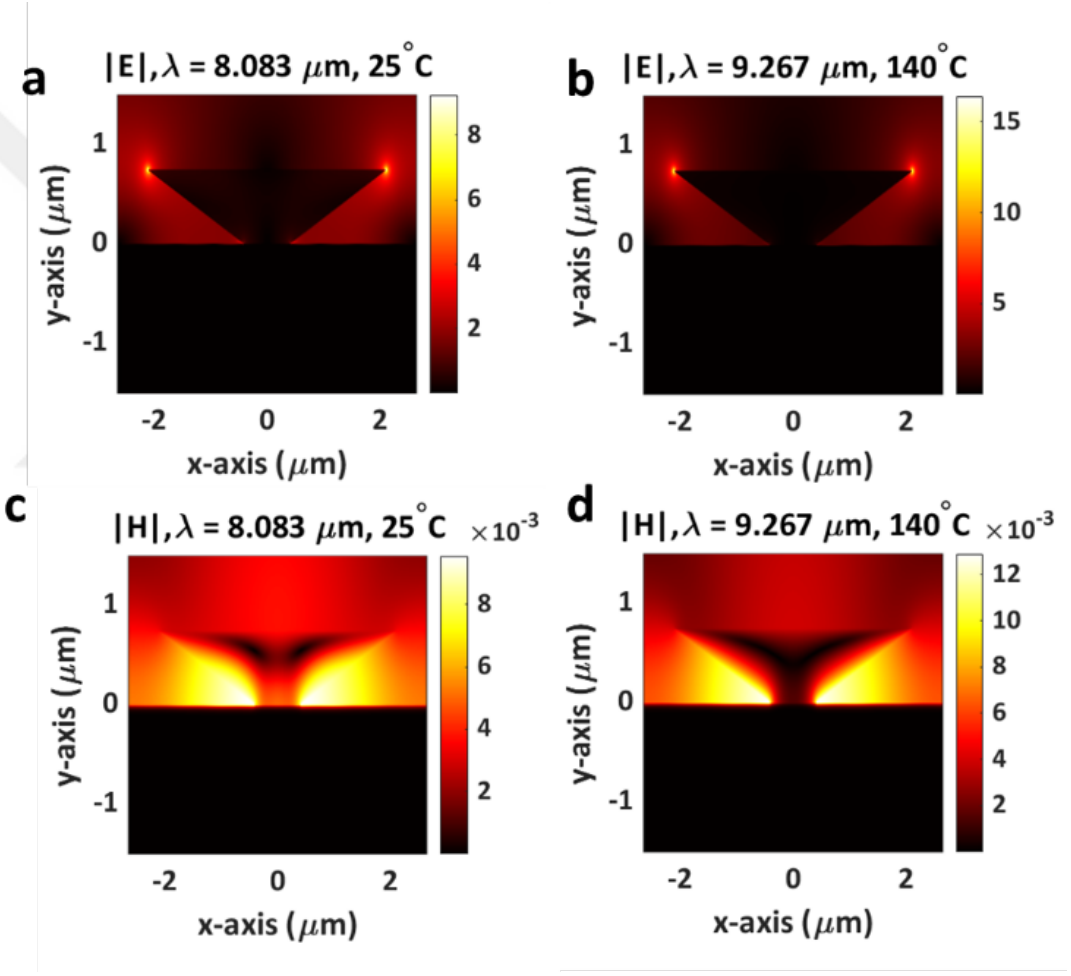

Figure 3.3: (a)-(b) Magnitude of E field, (c)-(d) Magnitude of H field for cold and hot phases at their respective resonance frequencies, $\boldsymbol{\lambda_C} = 8.083\ \mu m$ and $\boldsymbol{\lambda_H} = 9.267\ \mu m$

After this, the effect of $\boldsymbol{t}$, $\boldsymbol{b}$, and $\boldsymbol{h}$ on the absorption spectrum was investigated while keeping the $\boldsymbol{\alpha}$ constant. To conduct this study, the height of the structure is again varied between $\mathbf{650}$ nm to $\mathbf{850}$ nm while $\boldsymbol{t}$ and $\boldsymbol{b}$ also vary accordingly. As of the first study, a clear redshift on the resonance can be seen as the height of the structure increases. On the other hand, the resonance peaks get broadened due to the increased size of the structure.

In a third study, the effect of the filling ratio on the spectral response of the structure is investigated with scaling height as same as in the second study. In the spectral responses given in the third column of Fig.3.2, the effect of scaling is also the same as in the previous studies. It can be concluded that the resonance frequency is a strong function of the height and a weak function of the $\boldsymbol{\alpha}$. To prove this claim, for the fourth study, the height of the structure was chosen as $\mathbf{750}$ nm while the $\boldsymbol{t}$, $\boldsymbol{b}$, and $\boldsymbol{p}$ values are swept accordingly by keeping the filling ratio and $\boldsymbol{\alpha}$ constant. From the spectral responses presented in the rightmost column of Fig.3.2, it can be seen that the resonances are almost identical which shows that the governing mechanism behind this absorption is closely related to the filling ratio, $\boldsymbol{\alpha}$, and height of the structure, i.e. formation of a cavity between the inverse pyramid structure and the bottom reflector.

Fig.3.3 shows the magnitude of E and H field distributions over the optimized design at the respective resonance wavelengths of cold and hot phases. In both cases, there is a strong localization of the E field on the upper corners of the design. More importantly, it is clear that the H field localizes between the design and the bottom reflector. forming a Fabry-Perot cavity as also shown in the results of Fig.3.2 rightmost column [112, 113].

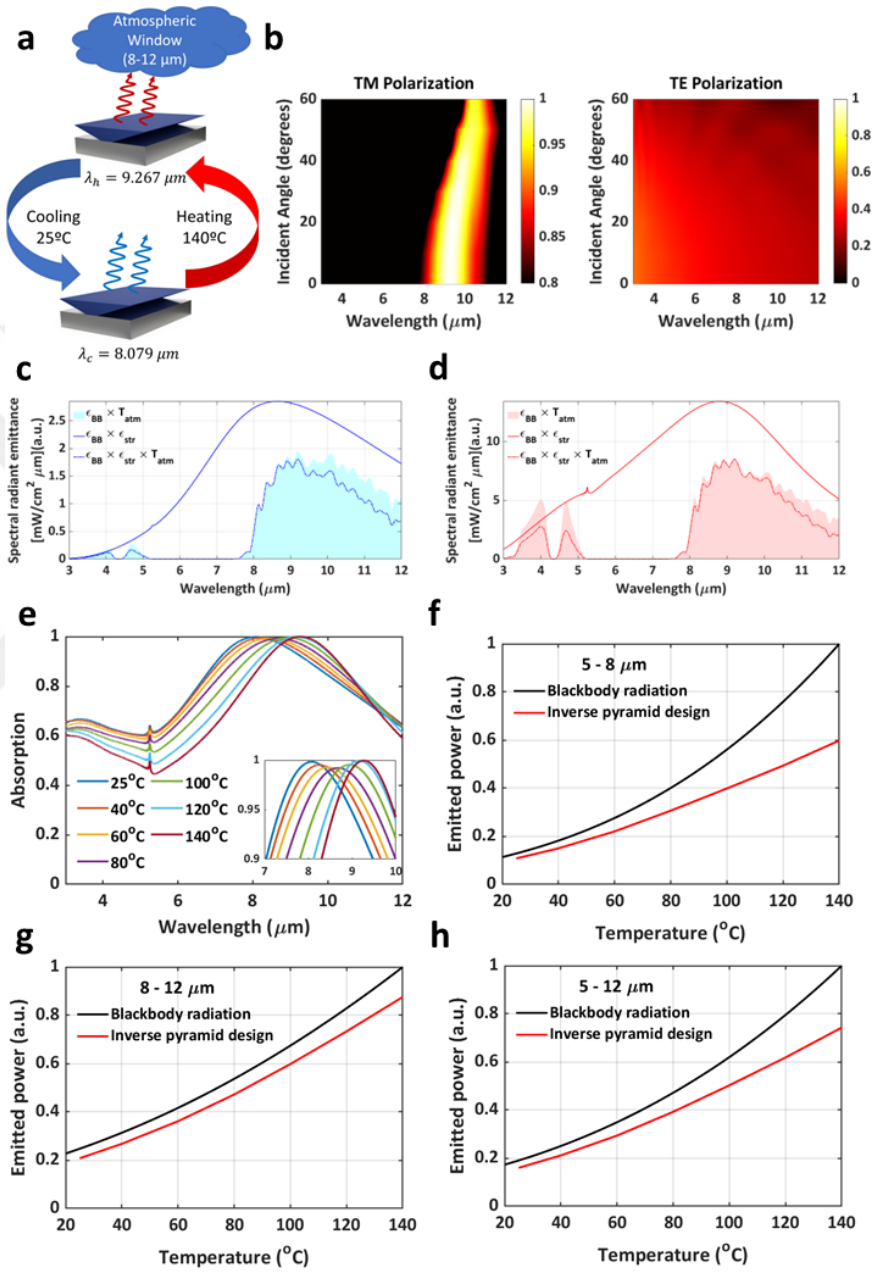

Figure 3.4: (a) Schematic representation of the radiative cooling process. (b) Absorption spectra of the structure under different incident angles at 140° C for TM and TE polarization. (c)-(d) Emitted radiative power of the structure with the atmospheric transparency windows at 25∘ C and 140° C. (e) Absorption spectra of the inverse pyramid design for different temperatures from 25° C to 140° C. Emitted power from the blackbody and inverse pyramid design over the wavelengths (f) $5-8\ \mu m$, (g) $8-12\ \mu m$, and (h) $5-12\ \mu m$.

To numerically verify and compare the emitted power density from the structure, the thermal emission model developed by Kocer et al. was used [114]. Using Kirchhoff's radiation law, emissivity from the surface can be written as

$$\epsilon_{eff}(\lambda, T) = \epsilon_{str}(\lambda, T) = 1 - R_{str}(\lambda, T) - T_{str}(\lambda, T) \tag{3.1}$$

where $\epsilon_{str}(\lambda, T)$, $R_{str}(\lambda, T)$, and $T_{str}(\lambda, T)$ are the absorptivity, reflectivity, and transmissivity of the structure which are a function of wavelength and the temperature. Due to the presence of an optically thick Ag bottom reflector, $T_{str}(\lambda, T)$ can be ignored; thus, the absorptivity can be written as:

$$\epsilon_{eff}(\lambda, T) = \epsilon_{str}(\lambda, T) = 1 - R_{str}(\lambda, T) \tag{3.2}$$

The radiation emitted from the surface of a blackbody can be written as (citation needed):

$$\epsilon_{blackbody}(\lambda, T) = \frac{2\pi hc^2}{\lambda^5} \frac{1}{e^{\frac{hc}{\lambda k_B T}} - 1} \tag{3.3}$$

where h, c and k_B are Planck constant, the speed of light in the vacuum and Boltzmann constant. The thermal emission of the surface can be found by multiplying Eq. 3.2 and Eq. 3.3:

$$\epsilon_{thermal}(\lambda, T) = \epsilon_{eff}(\lambda, T) \times \epsilon_{blackbody}(\lambda, T) \tag{3.4}$$

The optical power density is defined as the integral of the thermal emission for a given wavelength interval, which can be written as:

$$P_{optical} = \int_{\lambda_1}^{\lambda_2} \epsilon_{thermal}(\lambda, T) d\lambda \tag{3.5}$$

The average optical power density can be calculated as:

$$P_{avg} = \frac{\int_{\lambda_1}^{\lambda_2} \epsilon_{thermal}(\lambda, T) d\lambda}{\int_{\lambda_1}^{\lambda_2} \epsilon_{blackbody}(\lambda, T) d\lambda} \tag{3.6}$$

To investigate the isotropic response of the proposed structure, a set of simulations were conducted both in TM and TE polarization modes with varying

incident angles from 0 to 60 degrees. As seen from Fig.3.4(b) location of the resonance peak is not changing with respect to the incident angle upon an incident TM polarized wave. On the other hand, due to the asymmetric nature of the grating-like structures, the structure shows no resonance when the incident wave is TE polarized. After isotropic studies, using the extracted reflection data, the absorption spectra of the inverse pyramid design for temperatures varying from 25°C to 140° C were calculated, and with Eq. 3.4 the emitted power for each temperature was calculated for three different wavelength windows: $5-8\ \mu m$, $8-12\ \mu m$, and $5-12\ \mu m$ which are given in Fig.3.4(f), (g), and (h), respectively. From Fig.3.4(d) it is seen that the emitted power from the structure is almost identical to the blackbody over the $8-12\ \mu m$ window which is one of the atmospheric transparency windows.

Chapter 4

Conclusion & Future Outlook

In this thesis, we have demonstrated and discussed two different metasurfaces with tunable/adaptive optical responses, namely a graphene-based metasurface for active and broadband manipulation of terahertz radiation, and a phase-change-material based thermally tunable adaptive metasurface for radiative cooling applications. In each design, we kept simple elements to make fabrication processes easier yet kept the functionality of the design at the maximum level.

In Chapter 2, we have designed and analytically verified a novel and practically simplified graphene-based MPA that is capable of absorbing THz radiation within a 3 THz absorbing window. The broadband MPA, which comprises a periodic array of graphene patches with two different geometries on a metal-backed SiO_2 layer and supports propagating surface plasmon excitations in the broadband region, exhibits polarization-insensitive and omnidirectional absorption characteristics. Due to the tunable nature of graphene, it is possible to actively tune the absorption spectrum of the MPA from a resonant response to a broadband one and vice versa. Moreover, it is also possible to tune the spectral location of the absorption bandwidth by modifying the chemical potential of graphene. In an alternative approach, the absorption of the MPA can also be passively modified by adjusting the dimensions of the patches or thickness of the SiO_2 spacing layer.

Due to its simplified and novel design, it is expected that the proposed graphene-based MPA will find potential interest in THz spectroscopy and communications.

In Chapter 3, a thermally tunable metasurface based on a simple $SmNiO_3$ inverse pyramid grating as a PCM layer on top of an Ag bottom reflector was designed and its performance was investigated for adaptive radiative cooling applications. The thermal emission capabilities of the design were studied and verified using numerical simulations. The resulting design has an almost-identical emitted power to a blackbody over the wavelength window 8-12 μm in which the atmospheric absorption is minimal. Since the resonance element utilized in the design is a phase change material, the resonance blueshifts as the structure cools itself which makes the design adaptive to the ambient temperature. With these features, this design can easily be implemented in satellite, telecommunication applications without requiring any modulation to the cooling.

For future projects, we are planning to exploit the planar designs that have both radiative cooling and thermal camouflage properties, see Fig. 4.1 for initial results. This type of metasurfaces will be used for both cooling applications in electronic devices and may be in the new generation of 5G technologies as well as military applications for camouflaging the target from adversarial imaging technologies.

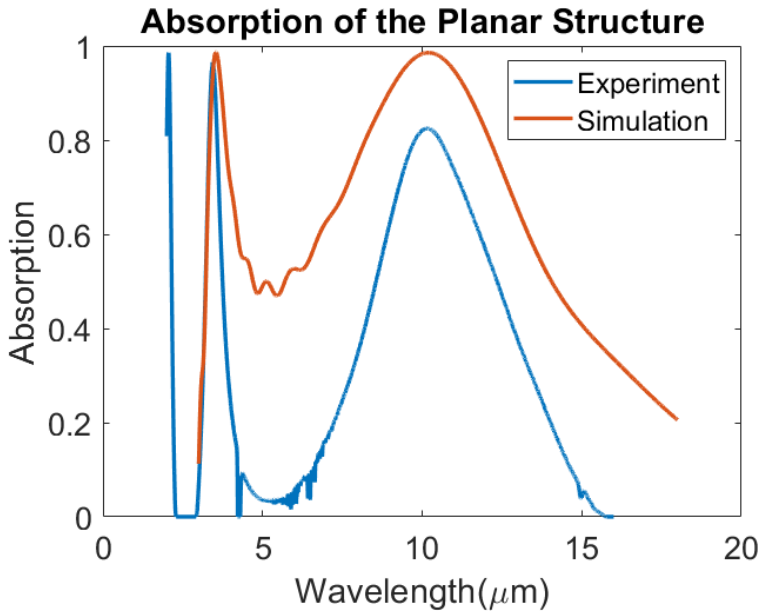

Figure 4.1: Experimental Absorption Measurement and Simulation Result of Future Planar Structure

Bibliography

[1] N. Engheta and R. W. Ziolkowski, eds., *Metamaterials*. Nashville, TN: John Wiley & Sons, June 2006.

[2] N. I. Zheludev and Y. S. Kivshar, "From metamaterials to metadevices," *Nature Materials*, vol. 11, pp. 917–924, Oct. 2012.

[3] R. Kshetrimayum, "A brief intro to metamaterials," *IEEE Potentials*, vol. 23, pp. 44–46, Jan. 2005.

[4] R. Hu, W. Xi, Y. Liu, K. Tang, J. Song, X. Luo, J. Wu, and C.-W. Qiu, "Thermal camouflaging metamaterials," *Materials Today*, vol. 45, pp. 120–141, May 2021.

[5] M. Kadic, G. W. Milton, M. van Hecke, and M. Wegener, "3d metamaterials," *Nature Reviews Physics*, vol. 1, pp. 198–210, Jan. 2019.

[6] W. Yang and Y.-S. Lin, "Tunable metamaterial filter for optical communication in the terahertz frequency range," *Optics Express*, vol. 28, p. 17620, May 2020.

[7] K. Wu, J.-J. Liu, Y. jiang Ding, W. Wang, B. Liang, and J.-C. Cheng, "Metamaterial-based real-time communication with high information density by multipath twisting of acoustic wave," *Nature Communications*, vol. 13, Sept. 2022.

[8] B. D. F. Casse, W. T. Lu, Y. J. Huang, E. Gultepe, L. Menon, and S. Sridhar, "Super-resolution imaging using a three-dimensional metamaterials nanolens," *Applied Physics Letters*, vol. 96, p. 023114, Jan. 2010.

[9] W. J. Padilla and R. D. Averitt, "Imaging with metamaterials," *Nature Reviews Physics*, vol. 4, pp. 85–100, Dec. 2021.

[10] T. Chen, S. Li, and H. Sun, "Metamaterials application in sensing," *Sensors*, vol. 12, pp. 2742–2765, Feb. 2012.

[11] F. Bagci, M. S. Gulsu, and B. Akaoglu, "Dual-band measurement of complex permittivity in a microwave waveguide with a flexible, thin and sensitive metamaterial-based sensor," *Sensors and Actuators A: Physical*, vol. 338, p. 113480, May 2022.

[12] N. Kida, T. Miyamoto, and H. Okamoto, "Emission of terahertz electromagnetic waves: A new spectroscopic method to investigate physical properties of solids," *Journal of the Physical Society of Japan*, vol. 91, Nov. 2022.

[13] W. Du, Y. Huang, Y. Zhou, and X. Xu, "Terahertz interface physics: from terahertz wave propagation to terahertz wave generation," *Journal of Physics D: Applied Physics*, vol. 55, p. 223002, Feb. 2022.

[14] A. Leitenstorfer, A. S. Moskalenko, T. Kampfrath, J. Kono, E. Castro-Camus, K. Peng, N. Qureshi, D. Turchinovich, K. Tanaka, A. G. Markelz, M. Havenith, C. Hough, H. J. Joyce, W. J. Padilla, B. Zhou, K.-Y. Kim, X.-C. Zhang, P. U. Jepsen, S. Dhillon, M. Vitiello, E. Linfield, A. G. Davies, M. C. Hoffmann, R. Lewis, M. Tonouchi, P. Klarskov, T. S. Seifert, Y. A. Gerasimenko, D. Mihailovic, R. Huber, J. L. Boland, O. Mitrofanov, P. Dean, B. N. Ellison, P. G. Huggard, S. P. Rea, C. Walker, D. T. Leisawitz, J. R. Gao, C. Li, Q. Chen, G. Valušis, V. P. Wallace, E. Pickwell-MacPherson, X. Shang, J. Hesler, N. Ridler, C. C. Renaud, I. Kallfass, T. Nagatsuma, J. A. Zeitler, D. Arnone, M. B. Johnston, and J. Cunningham, "The 2023 terahertz science and technology roadmap," *Journal of Physics D: Applied Physics*, vol. 56, p. 223001, Apr. 2023.

[15] M. Perenzoni and D. J. Paul, *Physics and applications of terahertz radiation*, vol. 173. Springer, 2014.

[16] G. Tzydynzhapov, P. Gusikhin, V. Muravev, A. Dremin, Y. Nefyodov, and I. Kukushkin, "New real-time sub-terahertz security body scanner," *Journal*

of Infrared, Millimeter, and Terahertz Waves, vol. 41, pp. 632–641, Mar. 2020.

[17] H. Feng, D. An, H. Tu, W. Bu, W. Wang, Y. Zhang, H. Zhang, X. Meng, W. Wei, B. Gao, and S. Wu, "A passive video-rate terahertz human body imager with real-time calibration for security applications," *Applied Physics B*, vol. 126, Aug. 2020.

[18] Y. Zhang, C. Wang, B. Huai, S. Wang, Y. Zhang, D. Wang, L. Rong, and Y. Zheng, "Continuous-wave THz imaging for biomedical samples," *Applied Sciences*, vol. 11, p. 71, Dec. 2020.

[19] Z. Yan, L.-G. Zhu, K. Meng, W. Huang, and Q. Shi, "THz medical imaging: from in vitro to in vivo," *Trends in Biotechnology*, vol. 40, pp. 816–830, July 2022.

[20] I. F. Akyildiz, C. Han, Z. Hu, S. Nie, and J. M. Jornet, "Terahertz band communication: An old problem revisited and research directions for the next decade," *IEEE Transactions on Communications*, vol. 70, pp. 4250–4285, June 2022.

[21] B. Chang, W. Tang, X. Yan, X. Tong, and Z. Chen, "Integrated scheduling of sensing, communication, and control for mmWave/THz communications in cellular connected UAV networks," *IEEE Journal on Selected Areas in Communications*, vol. 40, pp. 2103–2113, July 2022.

[22] T. Robin, C. Bouye, and J. Cochard, "Terahertz applications: trends and challenges," in *SPIE Proceedings* (L. P. Sadwick and C. M. O'Sullivan, eds.), SPIE, Mar. 2014.

[23] M. M. Hossain and M. Gu, "Radiative cooling: Principles, progress, and potentials," *Advanced Science*, vol. 3, p. 1500360, Feb. 2016.

[24] B. Zhao, M. Hu, X. Ao, N. Chen, and G. Pei, "Radiative cooling: A review of fundamentals, materials, applications, and prospects," *Applied Energy*, vol. 236, pp. 489–513, Feb. 2019.

[25] Z. Li, Q. Chen, Y. Song, B. Zhu, and J. Zhu, "Fundamentals, materials, and applications for daytime radiative cooling," *Advanced Materials Technologies*, vol. 5, p. 1901007, Feb. 2020.

[26] M. Chen, D. Pang, X. Chen, H. Yan, and Y. Yang, "Passive daytime radiative cooling: Fundamentals, material designs, and applications," *EcoMat*, vol. 4, Oct. 2021.

[27] H. Zhang and D. Fan, "Improving heat dissipation and temperature uniformity in radiative cooling coating," *Energy Technology*, vol. 8, p. 1901362, Mar. 2020.

[28] U. Banik, K. Sasaki, N. Reininghaus, K. Gehrke, M. Vehse, M. Sznajder, T. Sproewitz, and C. Agert, "Enhancing passive radiative cooling properties of flexible CIGS solar cells for space applications using single layer silicon oxycarbonitride films," *Solar Energy Materials and Solar Cells*, vol. 209, p. 110456, June 2020.

[29] J. Younes, K. Ghali, and N. Ghaddar, "Diurnal selective radiative cooling impact in mitigating urban heat island effect," *Sustainable Cities and Society*, vol. 83, p. 103932, Aug. 2022.

[30] N. Yu, P. Genevet, M. A. Kats, F. Aieta, J.-P. Tetienne, F. Capasso, and Z. Gaburro, "Light propagation with phase discontinuities: Generalized laws of reflection and refraction," *Science*, vol. 334, pp. 333–337, Oct. 2011.

[31] F. Aieta, P. Genevet, N. Yu, M. A. Kats, Z. Gaburro, and F. Capasso, "Out-of-plane reflection and refraction of light by anisotropic optical antenna metasurfaces with phase discontinuities," *Nano Letters*, vol. 12, pp. 1702–1706, Feb. 2012.

[32] F. Aieta, P. Genevet, M. A. Kats, N. Yu, R. Blanchard, Z. Gaburro, and F. Capasso, "Aberration-free ultrathin flat lenses and axicons at telecom wavelengths based on plasmonic metasurfaces," *Nano Letters*, vol. 12, pp. 4932–4936, Aug. 2012.

[33] M. Khorasaninejad, W. T. Chen, R. C. Devlin, J. Oh, A. Y. Zhu, and F. Capasso, "Metalenses at visible wavelengths: Diffraction-limited focusing and subwavelength resolution imaging," *Science*, vol. 352, pp. 1190–1194, June 2016.

[34] Z. Ma, S. M. Hanham, P. Albella, B. Ng, H. T. Lu, Y. Gong, S. A. Maier, and M. Hong, "Terahertz all-dielectric magnetic mirror metasurfaces," *ACS Photonics*, vol. 3, pp. 1010–1018, May 2016.

[35] V. Erçaglar, V. Erturk, A. Ghobadi, D. U. Yildirim, and E. Ozbay, "Numerical analysis of a thermally tunable spectrally selective absorber enabled by an all-dielectric metamirror," *Optics Letters*, vol. 45, p. 6174, Nov. 2020.

[36] O. V. Polischuk, V. S. Melnikova, and V. V. Popov, "Giant cross-polarization conversion of terahertz radiation by plasmons in an active graphene metasurface," *Applied Physics Letters*, vol. 109, p. 131101, Sept. 2016.

[37] T. Li, X. Hu, H. Chen, C. Zhao, Y. Xu, X. Wei, and G. Song, "Metallic metasurfaces for high efficient polarization conversion control in transmission mode," *Optics Express*, vol. 25, p. 23597, Sept. 2017.

[38] S. Sun, Z. Zhou, C. Zhang, Y. Gao, Z. Duan, S. Xiao, and Q. Song, "All-dielectric full-color printing with TiO_2 metasurfaces," *ACS Nano*, vol. 11, pp. 4445–4452, Mar. 2017.

[39] G. Zheng, H. Mühlenbernd, M. Kenney, G. Li, T. Zentgraf, and S. Zhang, "Metasurface holograms reaching 80% efficiency," *Nature Nanotechnology*, vol. 10, pp. 308–312, Feb. 2015.

[40] Q. Jiang, G. Jin, and L. Cao, "When metasurface meets hologram: principle and advances," *Advances in Optics and Photonics*, vol. 11, p. 518, Aug. 2019.

[41] X. Wang, Z. Nie, Y. Liang, J. Wang, T. Li, and B. Jia, "Recent advances on optical vortex generation," *Nanophotonics*, vol. 7, pp. 1533–1556, Aug. 2018.

[42] Y. Zhang, X. Yang, and J. Gao, "Orbital angular momentum transformation of optical vortex with aluminum metasurfaces," *Scientific Reports*, vol. 9, June 2019.

[43] M. Wei, Q. Xu, Q. Wang, X. Zhang, Y. Li, J. Gu, Z. Tian, X. Zhang, J. Han, and W. Zhang, "Broadband non-polarizing terahertz beam splitters with variable split ratio," *Applied Physics Letters*, vol. 111, p. 071101, Aug. 2017.

[44] F. Ding, R. Deshpande, C. Meng, and S. I. Bozhevolnyi, "Metasurface-enabled broadband beam splitters integrated with quarter-wave plate functionality," *Nanoscale*, vol. 12, no. 26, pp. 14106–14111, 2020.

[45] N. I. Landy, S. Sajuyigbe, J. J. Mock, D. R. Smith, and W. J. Padilla, "Perfect metamaterial absorber," *Physical Review Letters*, vol. 100, May 2008.

[46] N. Mattiucci, M. J. Bloemer, N. Aközbek, and G. D'Aguanno, "Impedance matched thin metamaterials make metals absorbing," *Scientific Reports*, vol. 3, Nov. 2013.

[47] H. Hajian, A. Ghobadi, B. Butun, and E. Ozbay, "Active metamaterial nearly perfect light absorbers: a review [invited]," *Journal of the Optical Society of America B*, vol. 36, p. F131, July 2019.

[48] K. B. Alici, F. Bilotti, L. Vegni, and E. Ozbay, "Experimental verification of metamaterial based subwavelength microwave absorbers," *Journal of Applied Physics*, vol. 108, p. 083113, Oct. 2010.

[49] J. W. Park, P. V. Tuong, J. Y. Rhee, K. W. Kim, W. H. Jang, E. H. Choi, L. Y. Chen, and Y. Lee, "Multi-band metamaterial absorber based on the arrangement of donut-type resonators," *Optics Express*, vol. 21, p. 9691, Apr. 2013.

[50] H.-T. Chen, "Interference theory of metamaterial perfect absorbers," *Optics Express*, vol. 20, p. 7165, Mar. 2012.

[51] Y. He, Q. Wu, and S. Yan, "Multi-band terahertz absorber at 0.1–1 THz frequency based on ultra-thin metamaterial," *Plasmonics*, vol. 14, pp. 1303–1310, Mar. 2019.

[52] S. Barzegar-Parizi and A. Khavasi, "Designing dual-band absorbers by graphene/metallic metasurfaces," *IEEE Journal of Quantum Electronics*, vol. 55, pp. 1–8, Apr. 2019.

[53] G. Yao, F. Ling, J. Yue, C. Luo, J. Ji, and J. Yao, "Dual-band tunable perfect metamaterial absorber in the THz range," *Optics Express*, vol. 24, p. 1518, Jan. 2016.

[54] N. Hu, F. Wu, L. an Bian, H. Liu, and P. Liu, "Dual broadband absorber based on graphene metamaterial in the terahertz range," *Optical Materials Express*, vol. 8, p. 3899, Nov. 2018.

[55] K. Aydin, V. E. Ferry, R. M. Briggs, and H. A. Atwater, "Broadband polarization-independent resonant light absorption using ultrathin plasmonic super absorbers," *Nature Communications*, vol. 2, Nov. 2011.

[56] M. G. Nielsen, A. Pors, O. Albrektsen, and S. I. Bozhevolnyi, "Efficient absorption of visible radiation by gap plasmon resonators," *Optics Express*, vol. 20, p. 13311, May 2012.

[57] F. Ding, J. Dai, Y. Chen, J. Zhu, Y. Jin, and S. I. Bozhevolnyi, "Broadband near-infrared metamaterial absorbers utilizing highly lossy metals," *Scientific Reports*, vol. 6, Dec. 2016.

[58] X. Chen, J. H. Wu, C. R. Liu, and P. Cao, "Ultra-broadband wide-angle perfect absorber in the visible regime through a thin grating–insulator–metal structure," *Journal of the Optical Society of America B*, vol. 36, p. 153, Jan. 2019.

[59] K. Gorgulu, A. Gok, M. Yilmaz, K. Topalli, N. Bıyıklı, and A. K. Okyay, "All-silicon ultra-broadband infrared light absorbers," *Scientific Reports*, vol. 6, Dec. 2016.

[60] L. Ye, Y. Chen, G. Cai, N. Liu, J. Zhu, Z. Song, and Q. H. Liu, "Broadband absorber with periodically sinusoidally-patterned graphene layer in terahertz range," *Optics Express*, vol. 25, p. 11223, May 2017.

[61] C. Liu, L. Qi, and X. Zhang, "Broadband graphene-based metamaterial absorbers," *AIP Advances*, vol. 8, p. 015301, Jan. 2018.

[62] P. Kumar, A. Lakhtakia, and P. K. Jain, "Graphene pixel-based polarization-insensitive metasurface for almost perfect and wideband terahertz absorption," *Journal of the Optical Society of America B*, vol. 36, p. F84, May 2019.

[63] L. Qi, C. Liu, and S. M. A. Shah, "A broad dual-band switchable graphene-based terahertz metamaterial absorber," *Carbon*, vol. 153, pp. 179–188, Nov. 2019.

[64] Z. Liu, L. Guo, and Q. Zhang, "A simple and efficient method for designing broadband terahertz absorber based on singular graphene metasurface," *Nanomaterials*, vol. 9, p. 1351, Sept. 2019.

[65] T. Wang, Y. Zhang, H. Zhang, and M. Cao, "Dual-controlled switchable broadband terahertz absorber based on a graphene-vanadium dioxide metamaterial," *Optical Materials Express*, vol. 10, p. 369, Jan. 2020.

[66] S. Quader, M. R. Akram, F. Xiao, and W. Zhu, "Graphene based ultra-broadband terahertz metamaterial absorber with dual-band tunability," *Journal of Optics*, vol. 22, p. 095104, Aug. 2020.

[67] A. Fardoost, F. G. Vanani, S. A. Amirhosseini, and R. Safian, "Design of multi-layer graphene based ultra wideband terahertz absorber," *IEEE Transactions on Nanotechnology*, pp. 1–1, 2016.

[68] S. Biabanifard, M. Biabanifard, S. Asgari, S. Asadi, and M. C. yagoub, "Tunable ultra-wideband terahertz absorber based on graphene disks and ribbons," *Optics Communications*, vol. 427, pp. 418–425, Nov. 2018.

[69] L. Liu, W. Liu, and Z. Song, "Ultra-broadband terahertz absorber based on a multilayer graphene metamaterial," *Journal of Applied Physics*, vol. 128, p. 093104, Sept. 2020.

[70] F. Ding, Y. Cui, X. Ge, Y. Jin, and S. He, "Ultra-broadband microwave metamaterial absorber," *Applied Physics Letters*, vol. 100, p. 103506, Mar. 2012.

[71] R. Badugu and J. R. Lakowicz, "Tamm state-coupled emission: Effect of probe location and emission wavelength," *The Journal of Physical Chemistry C*, vol. 118, pp. 21558–21571, Sept. 2014.

[72] M. G. Nielsen, D. K. Gramotnev, A. Pors, O. Albrektsen, and S. I. Bozhevolnyi, "Continuous layer gap plasmon resonators," *Optics Express*, vol. 19, p. 19310, Sept. 2011.

[73] X. Liu, T. Tyler, T. Starr, A. F. Starr, N. M. Jokerst, and W. J. Padilla, "Taming the blackbody with infrared metamaterials as selective thermal emitters," *Physical Review Letters*, vol. 107, July 2011.

[74] V. Erçağlar, H. Hajian, and E. Özbay, "VO_2–graphene-integrated hBN-based metasurface for bi-tunable phonon-induced transparency and nearly perfect resonant absorption," *Journal of Physics D: Applied Physics*, vol. 54, p. 245101, Mar. 2021.

[75] A. Gong, Y. Qiu, X. Chen, Z. Zhao, L. Xia, and Y. Shao, "Biomedical applications of terahertz technology," *Applied Spectroscopy Reviews*, vol. 55, pp. 418–438, Oct. 2019.

[76] C. Baker, W. R. Tribe, B. E. Cole, and M. C. Kemp, "The role of terahertz technology in security applications and people screening," in *Optical Terahertz Science and Technology*, OSA, 2005.

[77] J. Federici and L. Moeller, "Review of terahertz and subterahertz wireless communications," *Journal of Applied Physics*, vol. 107, p. 111101, June 2010.

[78] X. Ropagnol, M. Matoba, J. E. Nkeck, F. Blanchard, E. Isgandarov, J. Yumoto, and T. Ozaki, "Efficient terahertz generation and detection in cadmium telluride using ultrafast ytterbium laser," *Applied Physics Letters*, vol. 117, p. 181101, Nov. 2020.

[79] Z. Zhu, K. Cai, J. Deng, V. P. K. Miriyala, H. Yang, X. Fong, and G. Liang, "Electrical generation and detection of terahertz signal based on spin-wave emission from ferrimagnets," *Physical Review Applied*, vol. 13, Mar. 2020.

[80] H.-T. Chen, W. J. Padilla, J. M. O. Zide, A. C. Gossard, A. J. Taylor, and R. D. Averitt, "Active terahertz metamaterial devices," *Nature*, vol. 444, pp. 597–600, Nov. 2006.

[81] S. Wang, L. Kang, and D. H. Werner, "Hybrid resonators and highly tunable terahertz metamaterials enabled by vanadium dioxide (VO2)," *Scientific Reports*, vol. 7, June 2017.

[82] D. Chen, J. Yang, J. Huang, W. Bai, J. Zhang, Z. Zhang, S. Xu, and W. Xie, "The novel graphene metasurfaces based on split-ring resonators for tunable polarization switching and beam steering at terahertz frequencies," *Carbon*, vol. 154, pp. 350–356, Dec. 2019.

[83] M. Planck, "Ueber das gesetz der energieverteilung im normalspectrum," *Annalen der Physik*, vol. 309, pp. 553–563, 1901.

[84] S. Boltzmann, "Über die beziehung zwischen der wärmestrahlung und der temperatur," *Sitzungsber. Kaiserl. Akad. Wiss. Math. Naturwiss. Cl. II. Abth.*, vol. 79, pp. 391–428, 1879.

[85] G. Kirchhoff, "Über das verhältnis zwischen dem emissionsvermögen und dem absorptionsvermögen der körper für wärme und licht," 1978.

[86] Y. Qu, Q. Li, L. Cai, M. Pan, P. Ghosh, K. Du, and M. Qiu, "Thermal camouflage based on the phase-changing material gst," *Light: Science and Applications*, vol. 7, 2018.

[87] Y. Huang, M. Pu, Z. Zhao, X. Li, X. Ma, and X. Luo, "Broadband metamaterial as an "invisible" radiative cooling coat," *Optics Communications*, vol. 407, pp. 204–207, 2018.

[88] D. U. Yildirim, A. Ghobadi, M. C. Soydan, O. Atesal, A. Toprak, M. D. Caliskan, and E. Ozbay, "Disordered and densely packed ito nanorods as an excellent lithography-free optical solar reflector metasurface," *ACS Photonics*, vol. 6, pp. 1812–1822, 2019.

[89] L. Xiao, "Dual-band absorbers based on multiplexed gratings at mid-infrared frequencies," *Journal of Nanophotonics*, vol. 15, pp. 2–8, 2021.

[90] S. Chen, Z. Chen, J. Liu, J. Cheng, Y. Zhou, L. Xiao, and K. Chen, "Ultra-narrow band mid-infrared perfect absorber based on hybrid dielectric metasurface," *Nanomaterials*, vol. 9, 2019.

[91] M. Desouky, A. M. Mahmoud, and M. A. Swillam, "Silicon based mid-ir super absorber using hyperbolic metamaterial," *Scientific Reports*, vol. 8, pp. 8–15, 2018.

[92] A. Ghobadi, H. Hajian, B. Butun, and E. Ozbay, "Strong light-matter interaction in lithography-free planar metamaterial perfect absorbers," *ACS Photonics*, vol. 5, pp. 4203–4221, 2018.

[93] E. B. Boşdurmaz, H. Hajian, V. Erçağlar, and E. Özbay, "Graphene-based metasurface absorber for the active and broadband manipulation of terahertz radiation," *Journal of the Optical Society of America B*, vol. 38, p. C160, 2021.

[94] D. U. Yildirim, A. Ghobadi, M. C. Soydan, A. E. Serebryannikov, and E. Ozbay, "One-way and near-absolute polarization insensitive near-perfect absorption by using an all-dielectric metasurface," *Optics Letters*, vol. 45, p. 2010, 2020.

[95] H. H. Hsiao, C. H. Huang, B. T. Xu, G. T. Chen, and P. W. Ho, "Triple narrowband mid-infrared thermal emitter based on a au grating-assisted

nanoscale germanium/titanium dioxide distributed bragg reflector: Implications for molecular sensing," *ACS Applied Nano Materials*, vol. 4, pp. 9344–9352, 2021.

[96] K. Aydin, I. Bulu, and E. Ozbay, "Subwavelength resolution with a negative-index metamaterial superlens," *Applied Physics Letters*, vol. 90, 2007.

[97] A. Erentok and R. W. Ziolkowski, "Metamaterial-inspired efficient electrically small antennas," *IEEE Transactions on Antennas and Propagation*, vol. 56, pp. 691–707, 3 2008.

[98] M. A. Kats, R. Blanchard, P. Genevet, Z. Yang, M. M. Qazilbash, D. N. Basov, S. Ramanathan, and F. Capasso, "Thermal tuning of mid-infrared plasmonic antenna arrays using a phase change material," *Optics Letters*, vol. 38, p. 368, 2013.

[99] W. Dong, Y. Qiu, X. Zhou, A. Banas, K. Banas, M. B. Breese, T. Cao, and R. E. Simpson, "Tunable mid-infrared phase-change metasurface," *Advanced Optical Materials*, vol. 6, pp. 1–6, 2018.

[100] A. K. U. Michel, D. N. Chigrin, T. W. Maß, K. Schönauer, M. Salinga, M. Wuttig, and T. Taubner, "Using low-loss phase-change materials for mid-infrared antenna resonance tuning," *Nano Letters*, vol. 13, pp. 3470–3475, 2013.

[101] A. K. Osgouei, H. Hajian, B. Khalichi, A. E. Serebryannikov, A. Ghobadi, and E. Ozbay, "Active tuning from narrowband to broadband absorbers using a sub-wavelength vo2 embedded layer," *Plasmonics*, vol. 16, pp. 1013–1021, 8 2021.

[102] M. A. Kats, D. Sharma, J. Lin, P. Genevet, R. Blanchard, Z. Yang, M. M. Qazilbash, D. N. Basov, S. Ramanathan, and F. Capasso, "Ultra-thin perfect absorber employing a tunable phase change material," *Applied Physics Letters*, vol. 101, 11 2012.

[103] S. Abdollahramezani, O. Hemmatyar, H. Taghinejad, A. Krasnok, Y. Kiarashinejad, M. Zandehshahvar, A. Alù, A. Alù, and A. Adibi, "Tunable nanophotonics enabled by chalcogenide phase-change materials," *Nanophotonics*, 2020.

[104] E. Buhara, A. Ghobadi, B. Khalichi, H. Kocer, and E. Ozbay, "Mid-infrared adaptive thermal camouflage using a phase-change material coupled dielectric nanoantenna," *Journal of Physics D: Applied Physics*, vol. 54, 2021.

[105] Lumerical Inc., "https://www.lumerical.com/products/,"

[106] L. A. Falkovsky, "Optical properties of graphene," *Journal of Physics: Conference Series*, vol. 129, p. 012004, Oct. 2008.

[107] E. Palik, *Handbook of Optical Constants of Solids*. Academic Press handbook series, Elsevier Science, 1998.

[108] Z. Fang, S. Thongrattanasiri, A. Schlather, Z. Liu, L. Ma, Y. Wang, P. M. Ajayan, P. Nordlander, N. J. Halas, and F. J. G. de Abajo, "Gated tunability and hybridization of localized plasmons in nanostructured graphene," *ACS Nano*, vol. 7, pp. 2388–2395, Feb. 2013.

[109] Lumerical Inc., "https://www.lumerical.com/products/,"

[110] D. R. Lide, "Crc handbook of chemistry and physics," *Journal of Molecular Structure*, vol. 268, p. 320, 1992.

[111] A. Shahsafi, P. Roney, Y. Zhou, Z. Zhang, Y. Xiao, C. Wan, R. Wambold, J. Salman, Z. Yu, J. Li, J. T. Sadowski, R. Comin, S. Ramanathan, and M. A. Kats, "Temperature-independent thermal radiation," *Proceedings of the National Academy of Sciences*, vol. 116, pp. 26402–26406, 2019.

[112] H. T. Miyazaki and Y. Kurokawa, "Controlled plasmon resonance in closed metal/insulator/metal nanocavities," *Applied Physics Letters*, vol. 89, 2006.

[113] C.-W. Cheng, M. N. Abbas, Z.-C. Chang, M. H. Shih, C.-M. Wang, M. C. Wu, and Y.-C. Chang, "Angle-independent plasmonic infrared band-stop reflective filter based on the ag=sio 2 =ag t-shaped array," 2011.

[114] H. Kocer, M. C. Cakir, Y. Durna, M. C. Soydan, O. Odabasi, H. Isik, K. Aydin, and E. Ozbay, "Exceptional adaptable mwir thermal emission for ordinary objects covered with thin vo2 film," *Journal of Quantitative Spectroscopy and Radiative Transfer*, vol. 262, p. 107500, 2021.

[115] M. Esfandyarpour, E. C. Garnett, Y. Cui, M. D. McGehee, and M. L. Brongersma, "Metamaterial mirrors in optoelectronic devices," *Nature Nanotechnology*, vol. 9, pp. 542–547, June 2014.

Appendix A

Code

A.1 Reflection Phase Extraction Using Lumerical and MATLAB

In this section, we are going to demonstrate how to extract reflection phase information from Lumerical FDTD Solutions [105] by reproducing the Figure 1 (g) from the paper by Esfandyarpour et al. [115]. In this paper, authors extract the reflection phase of a metamaterial structure consisting of a gold grating with respect to the depth of the grating. The simulation setup, can be seen in Fig.A.1. After setting the parameters, such as the simulation frequency, and the sweep parameter such as the grove height, we should extract the phase of non zero E-field (in our case x-component) in the point monitor located at Z_m. Although, one can use this raw phase information which is sum of the reflection phase and the phase of propagation, an important point to note is that we should subtract the phase gained due to propagation of the plane wave. This phase can be calculated as:

$$\theta_{path} = \frac{|Z_m - Z_d| + |Z_s - Z_d|}{\lambda} \tag{A.1}$$

where λ is the wavelength of interest. So using, a MATLAB script, one can extract the reflection phase caused by the metamaterial. The resulting reproduction of

Figure 1 (g) [115] can be seen in Fig.A.2.

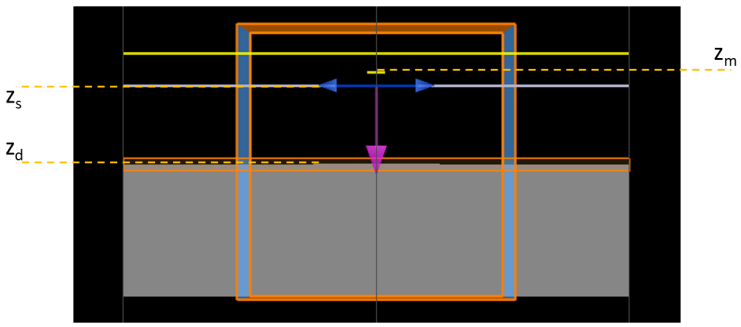

Figure A.1: Lumerical Simulation Setup for Reflection Phase Extraction, Z_m, Z_s, and Z_d are the z-coordinates of the reflection point monitor, plane wave source, and the metamaterial top surface respectively.

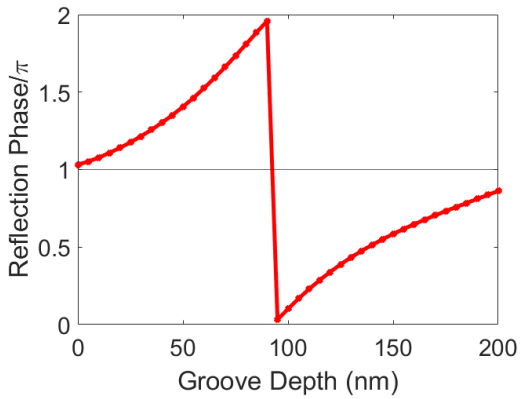

Figure A.2: Reproduction of Figure 1 (g) from [115], using Lumerical and MATLAB.